

## RESEARCH ARTICLE

10.1002/2014JB011277

## Key Points:

- Creep in sands controls phenomena like production-induced reservoir compaction
- Creep is dominated by subcritical crack growth, leading to grain failure
- In the presence of aqueous fluids, stress corrosion controls crack growth

## Correspondence to:

S. J. T. Hangx,  
s.j.t.hangx@uu.nl

## Citation:

Brzesowsky, R. H., S. J. T. Hangx, N. Brantut, and C. J. Spiers (2014), Compaction creep of sands due to time-dependent grain failure: Effects of chemical environment, applied stress, and grain size, *J. Geophys. Res. Solid Earth*, 119, doi:10.1002/2014JB011277.

Received 13 MAY 2014

Accepted 22 SEP 2014

Accepted article online 24 SEP 2014

## Compaction creep of sands due to time-dependent grain failure: Effects of chemical environment, applied stress, and grain size

R. H. Brzesowsky<sup>1,2</sup>, S. J. T. Hangx<sup>1</sup>, N. Brantut<sup>3</sup>, and C. J. Spiers<sup>1</sup>

<sup>1</sup>HPT Laboratory, Faculty of Geosciences, Utrecht University, Utrecht, Netherlands, <sup>2</sup>Now at Philips Research, High Tech Campus, Eindhoven, Netherlands, <sup>3</sup>Rock and Ice Physics Laboratory, Department of Earth Sciences, University College London, London, UK

**Abstract** Time-dependent brittle creep plays a role in controlling compaction of sands and sandstones under upper crustal conditions, influencing phenomena such as production-induced reservoir compaction, surface subsidence, and induced seismicity. Brittle creep also plays a role in determining the mechanical behavior of gouge-rich faults. We performed uniaxial creep experiments on sand to investigate the effects of chemical environment (dry versus solution flooded), grain size ( $d = 196\text{--}378\ \mu\text{m}$ ), and applied effective stress ( $\sigma_a$  up to 30 MPa), at room temperature conditions favoring grain-scale brittle processes. Creep measurements were complemented with acoustic emission (AE) detection and microstructural analysis to characterize the main creep mechanism. Wet samples showed much higher creep strains than dry-tested samples. AE event counts showed a direct relation between grain failure and creep strain, with higher AE rates occurring in the wet samples. Therefore, we inferred that time-dependent deformation was dominated by subcritical crack growth, resulting in grain failure accompanied by intergranular sliding rearrangements, and that crack growth in the presence of chemically active fluids was controlled by stress corrosion. The sensitivity of the compaction rate of the sands to  $d$  and  $\sigma_a$  can be expressed as  $\dot{\epsilon} \propto d^i \sigma_a^j$  where  $i \approx 6$  and  $j \approx 21$  under dry conditions and  $i \approx 9$  and  $j \approx 15$  under wet conditions. Our results were compared to a simple model based on Hertzian contact theory, linear elastic fracture mechanics, and subcritical crack growth. This model showed agreement between the observed stress and grain size sensitivities of creep, within a factor of 2.

### 1. Introduction

The time-independent, or short-term, compaction behavior of dry and wet sands has been extensively investigated, both in the laboratory and from a micromechanical modeling point of view, and has been shown to primarily involve grain fracture and rearrangement processes, with relatively little effect of pore fluids [Brzesowsky *et al.*, 2014; Chester *et al.*, 2004; Chuhan *et al.*, 2002, 2003; Hangx *et al.*, 2010; Lambe and Whitman, 1979; Liu *et al.*, 1993]. However, it is commonly observed, in experiments at 20 to 200–300°C, that pore fluids enhance the kinetics of subcritical grain cracking mechanisms, as well as promoting processes such as pressure solution [Atkinson and Meredith, 1987; Brantut *et al.*, 2013; Costin, 1989; de Boer, 1977; Dunning *et al.*, 1994; Elias and Hajash, 1992; Hangx *et al.*, 2010; Renard *et al.*, 1999; Schutjens, 1991a, 1991b; Zhang *et al.*, 1990a, 1990b]. This implies that time-dependent compaction creep may be important in sands and sandstones under natural, even upper crustal, conditions [De Waal, 1986].

On the basis of microstructural evidence and extrapolation of the above experimental results, it is indeed widely accepted that time-dependent compaction creep processes play a role in controlling the porosity and permeability evolution of clastic sediments deposited in subsiding basin settings [Donaldson *et al.*, 1995; Karner *et al.*, 2005; Schutjens, 1991a; Zhang *et al.*, 1990a]. Further evidence for the possible operation of such creep processes under upper crustal conditions is provided by the fact that groundwater extraction and hydrocarbon production frequently lead to surface subsidence and induced seismicity, which may continue after production has ceased [Doornhof *et al.*, 2006; Hettema *et al.*, 2002; Schutjens *et al.*, 1994, 1995], though several other processes could contribute too. Brittle creep processes operating on the grain scale also play an important role in controlling compaction, strength recovery, and slip stability of fault gouges, thus influencing the seismogenic behavior of faults as well as postseismic stress redistribution and earthquake aftershock behavior [Anderson and Grew, 1977; Main and Meredith, 1991; Scholz, 1968]. In addition, the creep properties of upper crustal rocks strongly affect the hydraulic

fracturing behavior of gas-bearing shales [Sone and Zoback, 2010], geothermal reservoirs [Anderson and Grew, 1977], and tight sandstones.

Despite the important implications of creep in understanding (production-induced) reservoir compaction, previous experimental studies have not investigated the effect of applied stress and grain size on the long-term compaction creep behavior of sands systematically. It is expected that the presence of water strongly enhances subcritical crack growth [Atkinson and Meredith, 1981; Darot and Gueguen, 1986; Dunning *et al.*, 1994], but how this controls creep in granular rocks and the role played by the chemical environment are poorly known. Previous experimental work indicates that creep effects may be important in controlling the long-term compaction behavior of sands. However, few constitutive laws, accounting for the physical and chemical processes that act on the grain scale, have yet been put forward for compaction creep behavior of sands [Brzesowsky, 1995] and sandstones [Brantut *et al.*, 2012, 2013].

In this paper, we systematically investigate the compaction creep behavior of sands, focusing on the effect of chemical environment, applied stress, and grain size. Acoustic emission (AE) detection and microstructural methods are used to gain insight into the operating microphysical mechanisms. Finally, we design a simple model based on the basic principles of Hertzian theory and linear elastic fracture mechanics, coupled to stress corrosion cracking, in order to link our macroscopic creep data to the microscale, subcritical crack growth processes operating.

## 2. Experimental Techniques

The experiments consisted of a series of 37 uniaxial, oedometer-type compaction creep experiments performed on sands under both dry and wet (drained) conditions. For the drained tests, we used aqueous pore fluids of varying salinity, as well as inert pore fluids for control purposes. Applied stress and grain size were independently varied to determine their effects on the creep behavior of sands as well. For our experiments, we used an oedometer rather than a hydrostatic compaction apparatus, as the former allows intrinsically better control and measurement of initial (i.e., before testing) sample porosity. Two series of experiments were performed:

1. Two-stage creep tests, during which the samples were first subjected to load cycling under dry conditions ramping the applied stress ( $\sigma_a$ ) throughout the range  $0.24 \leq \sigma_a \leq 21.7$  or  $0.24 \leq \sigma_a \leq 30.0$  MPa and using constant loading rates of 282 or 390 MPa/h, corresponding to mean loading strain rates of  $\sim 10^{-4} \text{ s}^{-1}$ , i.e., the strain rate during active load ramping. Cycling was terminated by arresting the loading ramp at a creep stage stress of 7.2, 10.9, 14.5, 18.1, 20.0, 21.7, or 30.0 MPa. After allowing compaction creep under dry conditions until creep rates diminished to values below  $10^{-8} \text{ s}^{-1}$  (mainly after  $\sim 2$  days), the samples were then flooded with pore fluid at the same stress, leading to a creep stage under wet conditions. In all, 30 such tests were performed using three different grain size batches ( $196 \pm 16 \mu\text{m}$ ,  $275 \pm 25 \mu\text{m}$ , and  $378 \pm 22 \mu\text{m}$ ). The applied maximum effective creep stresses were equivalent to a burial depth or reservoir depth of 2.5–3 km, assuming a hydrostatic pore pressure.
2. Single-stage creep tests performed on samples flooded with pore fluid at the initial “set point” stress and directly loaded (i.e., under wet conditions) to the desired creep stress (10.0, 20.0, or 30.0 MPa), using a constant loading rate of 5495 MPa/h, corresponding to a mean loading strain rate of  $\sim 10^{-3} \text{ s}^{-1}$ . Though this strain is about 1 order of magnitude higher than those of the first series of experiments, it has been shown that loading rate or chemical environment does not significantly affect loading (time-independent) strain [see Brzesowsky *et al.*, 2014, Figure 4]. A total of seven tests were performed on a fixed grain size batch ( $d = 275 \pm 25 \mu\text{m}$ ), with the aim of assessing the effect of chemical environment on stress-strain behavior.

### 2.1. Starting Material and Sample Preparation

The sand used in these experiments is the same as that used by Brzesowsky *et al.* [2011] and was obtained from fresh samples taken from the Heksenberg Formation, Beaujean quarry, Heerlen, Netherlands [see also Brzesowsky *et al.*, 2011, 2014]. X-ray diffraction analysis and inductively coupled plasma emission spectroscopy (ICP-ES) measurements indicate a quartz content of  $> 99$  wt % with zircon and Na-rich feldspar present as principal trace minerals. In reflected light, some sand grains ( $< 0.5\%$ ) show a thin surface layer of iron oxide/hydroxide, as supported by a 0.02 wt % Fe ICP-ES measurement. Scanning electron microscopy (SEM) showed that most sand grains are subrounded and have a generally smooth surface with local, pitted patches

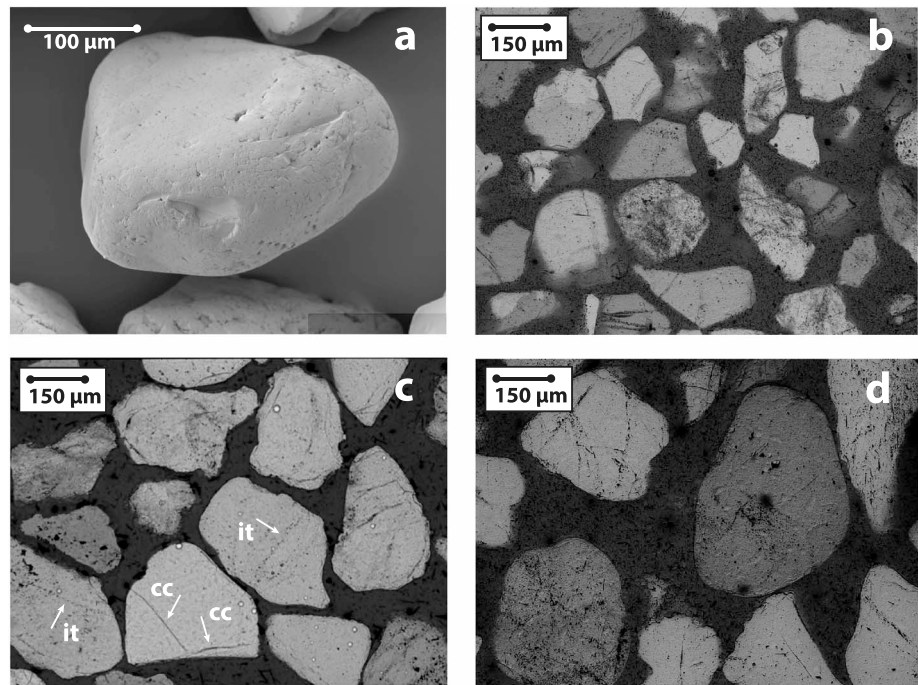


**Figure 1.** Micrographs of the Heksenberg undeformed sand. (a) SEM micrograph showing a close-up of a single grain (grain size fraction  $275 \pm 25 \mu\text{m}$ ), showing that most sand grains appear as subrounded and show a generally smooth surface with patches of pits, grooves/scratches, and depressions created by broken-out pieces. (b) Micrograph of grain size fraction  $196 \pm 16 \mu\text{m}$ . (c) Micrograph of grain size fraction  $275 \pm 25 \mu\text{m}$ , showing the closed intragranular cracks (cc) and inclusion trails (it). (d) Micrograph of grain size fraction  $378 \pm 22 \mu\text{m}$ .

(diameter  $\sim 20\text{--}50 \mu\text{m}$ ), characterized by rounded and triangular pits (dimension  $\sim 5\text{--}15 \mu\text{m}$ ), as can be seen in Figure 1a. Grooves (dimension  $\sim 5 \times 50 \mu\text{m}$ ) and depressions (dimension  $\sim 50 \mu\text{m}$ ) apparently corresponding to spalled-out fragments are also locally present (see Figure 1a). With reference to Figures 1b–1d (sieved fraction), thin section analysis showed that  $\sim 97\text{--}98\%$  of the grains is monocrystalline and subrounded, i.e., ranging from subangular to rounded. The majority of these grains ( $\sim 60\%$ ) contains intersecting patterns of inclusion trails, which are inferred to originate from healed intragranular cracks, while only a few ( $\sim 10\%$ ) exhibit “closed,” nonhealed intragranular cracks subparallel to the inclusion trails (see Figures 1b–1d).

Fractions of the sand, with grain sizes of  $196 \pm 16$ ,  $275 \pm 25$ , and  $378 \pm 22 \mu\text{m}$ , were prepared by sieving (Figures 1b–1d). From the sieved fractions, the feldspar trace material was successfully removed using two gravitational separation methods: (1) applying a heavy liquid (bromoform) separation technique ( $196 \pm 16 \mu\text{m}$  and  $378 \pm 22 \mu\text{m}$  fractions) or (2) by washing in water ( $275 \pm 25 \mu\text{m}$  fraction). Analysis of images of the three fractions reported by Brzesowsky *et al.* [2011] showed that grain roundness, and hence the radius of curvature of grain asperities, increased with increasing grain size [see Brzesowsky *et al.*, 2011, Figure 9]. This is in line with relationships known in sedimentary petrology and has been attributed to more effective abrasion of larger-sized particles [Donaldson *et al.*, 1995].

Presaturated silica solution was prepared by dissolving a fixed mass of sodium metasilicate ( $\text{Na}_2\text{SiO}_3 \cdot 9\text{H}_2\text{O}$ ) in order to yield an equilibrium  $\text{SiO}_2$  concentration ( $\sim 6$  ppm at  $25^\circ\text{C}$  and  $0.1$  MPa fluid pressure) [Hicks, 1989; Morey *et al.*, 1962; Rimstidt and Barnes, 1980; Robie *et al.*, 1978; Schutjens, 1991a; Walther and Helgeson, 1977]. Subsequently, a small quantity of  $0.1$  M hydrochloric acid solution was added to obtain a pH between 6 and 7. The composition of the fluid at this point is estimated to be  $6.3$  ppm  $\text{SiO}_2$  and  $\sim 2 \cdot 10^{-4}$  M NaCl. Before use, silica saturation was attained by allowing the pore fluid to circulate in a closed polyefine container containing an excess of quartz sand. In addition, tests were performed using *n*-decane (four in total) as pore fluid, as well as with silica-saturated saline solution. The saline solution was prepared by adding NaCl to silica-saturated solution, as prepared above. Two tests were performed using  $1$  M NaCl solution and another two tests with  $6.15$  M NaCl solution.

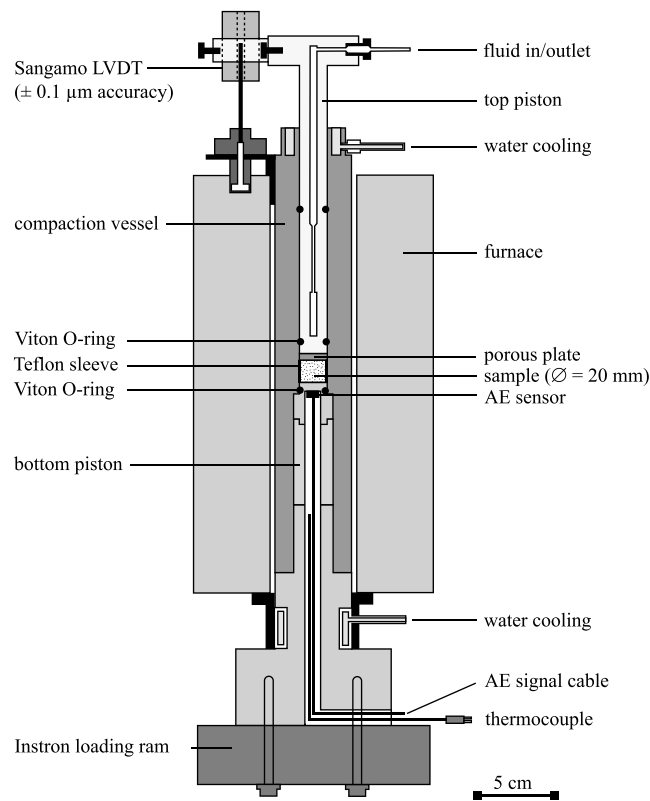


**Figure 2.** Semischematic diagram showing the uniaxial deformation apparatus used in the present compaction creep experiments on sands.

in/outlet in the top piston. A Teflon ring behind this porous plate prevents sand grains from passing between the vessel wall and the top piston. Sealing of the top and bottom pistons is achieved using Viton O-rings, lubricated using Molykote III compound silicon grease.

Force applied to the top piston is measured externally using the Instron load cell (10 kN range, resolution  $\pm 0.025$  kN). Piston position and displacement are measured using both an LVDT (linear variable differential transformer, range  $\pm 50$  mm, resolution  $\pm 2.5$   $\mu\text{m}$ ) located in the Instron drive unit and a Sangamo LVDT (range  $\pm 5$  mm, resolution  $\pm 0.1$   $\mu\text{m}$ ) located between the upper piston and the vessel. Sample temperature is measured using a sheathed type-K (chromel/alumel) thermocouple (resolution  $0.05^\circ\text{C}$ ) embedded in the vessel wall and electrically isolated with respect to the piston bore wall by a thin layer of Teflon (Figure 2).

In order to detect grain-scale brittle failure events, acoustic emissions were counted using an acoustic emission (AE) monitoring system. To detect AE emissions, an AE sensor (lead zirconate titanate, ceramic piezoelectric resonator) is located in the upper section of the bottom piston [Brzesowsky, 1995; Hangx et al., 2010]. The system used enables sensing, amplification, frequency filtering, discrimination, and counting of wave packets emanating from microseismic events within the sample but no determination of AE energies. This is connected to a precision preamplifier (36 dB gain) and a multistage signal conditioning system, the latter providing 24 dB gain and incorporating a 100 kHz to 1 MHz band-pass filter to eliminate low-frequency interference and sensor resonance effects. Events are counted using two counter channels, for which a constant discrimination trigger threshold in the range of 125 to 700 mV was set, just above noise level. Pulse stretching times (PSTs) for the two channels were set at 530 and 1000  $\mu\text{s}$ , or to 530 and 2450  $\mu\text{s}$ , which served as a check for wave packet arrival-bunching effects and counter saturation. For well-spaced events, the count rates obtained by the two channels should be identical. AE waveforms observed during dry and wet compaction creep of sand typically endure for 0.75 and 0.25 ms respectively before the last retriggering. Consequently, the maximum AE event rates countable by the AE system are estimated to be 800 and 1300 Hz for dry and wet material, respectively.

## 2.2. Experimental Setup and Acoustic Emissions Monitoring

The compaction experiments were performed using an Instron 1362 servo-controlled testing machine, equipped with a 1-D (uniaxial) compaction vessel (Figure 2). In this loading geometry, the sample undergoes uniaxial strain. The applied axial stress is the maximum principal stress  $\sigma_1$ , while for loose granular samples [Karig and Hou, 1992] the lateral stresses ( $\sigma_2 = \sigma_3$ ) are generally smaller than  $\sigma_1$ , provided wall friction is low.

The vessel used in our experiments is a modified version of the oedometer described by Schutjens [1991a] [see also Hangx et al., 2010]. The vessel and loading pistons are constructed from Monel K-500, a corrosion-resistant copper-nickel alloy, employed to minimize sample contamination by corrosion. The bottom piston is fixed within the vessel. The moveable top piston contains a pore fluid bore and is tipped with a porous plate, enabling evacuation of the sample or fluid to enter the sample through the fluid

**Table 1.** Overview of the Two-Stage Creep Tests Performed on Sands at Room Temperature<sup>a</sup>

Expt.	$\sigma_a$ (MPa)	$d$ ( $\mu\text{m}$ )	Dry Creep Stage			Flooded Creep Stage		
			$\varphi_i$ (%)	Condition	Time (days)	$\varphi_i$ (%)	Condition <sup>c</sup>	Time (days)
<i>Precompaction Stress, <math>\sigma_i = 30</math> MPa</i>								
BS2	30	275 ± 25	37.5	evacuated	4	37.1	n.a.	n.a.
BS3	30	275 ± 25	37.5	evacuated	0.03	37.1	aq. solution	5
BS4	30	275 ± 25	37.0	evacuated	0.03	36.6	1 M NaCl	5
BS5	30	275 ± 25	37.8	vacuum dried <sup>b</sup>	2	37.1	aq. solution	10
BS6	30	275 ± 25	37.6	vacuum dried <sup>b</sup>	2	36.7	1 M NaCl	10
BS7	30	275 ± 25	38.0	evacuated	4	37.0	n.a.	n.a.
BS9	30	275 ± 25	37.4	evacuated	2	36.7	aq. solution	24
BS10 and BS44	30	275 ± 25	37.1; 37.6	vacuum dried	7; 2	36.5; 36.9	n.a.	n.a.
BS11, BS30, and BS31	30	275 ± 25	37.6; 37.5; 37.3	vacuum dried	2	37.0; 36.7; 36.2	aq. solution	16; 9; 10
BS13	20	275 ± 25	38.2	vacuum dried	2	38.1	aq. solution	9
<i>Precompaction Stress, <math>\sigma_i = 21.7</math> MPa</i>								
BS35 and BS36	21.7	275 ± 25	39.1; 39.1	vacuum dried	2	38.7; 38.7	<i>n</i> -decane	6; 8
BS29 and BS32	21.7	275 ± 25	39.2; 39.1	vacuum dried	2	38.7; 38.6	aq. solution	8; 11
BS19 and BS20	21.7	275 ± 25	39.0; 39.0	vacuum dried	2	38.6; 38.6	6.15 M NaCl	13; 9
BS22 and BS23	18.1	275 ± 25	39.4; 39.2	vacuum dried	2	39.2; 39.1	aq. solution	10; 11
BS15 and BS21	14.5	275 ± 25	39.3; 39.4	vacuum dried	2	39.2; 39.3	aq. solution	10; 7
BS18	10.9	275 ± 25	39.7	vacuum dried	2	39.7	aq. solution	2
BS16 and BS17	7.2	275 ± 25	39.7; 39.6	vacuum dried	2	39.7; 39.6	aq. solution	4; 5
BS24 and BS25	21.7	196 ± 16	39.6; 39.5	vacuum dried	2	39.3; 39.2	aq. solution	9; 8
BS27 and BS28	21.7	378 ± 22	38.4; 38.1	vacuum dried	2	37.7; 37.4	aq. solution	13; 8

<sup>a</sup>Symbols:  $\sigma_i$  is the precompaction stress, i.e., the maximum applied stress before creep (MPa);  $\sigma_a$  is the applied stress during both creep stages (MPa);  $d$  is grain size ( $\mu\text{m}$ ); and  $\varphi_i$  is the porosity at the start of the creep stage (%).

<sup>b</sup>Drying agent was  $\text{P}_2\text{O}_5$  (phosphorous pentoxide).

<sup>c</sup>The aqueous solution consisted of distilled water saturated with silica; n.a. = not applicable.

### 2.3. Testing Procedure

Prior to each test, the vessel was fully assembled, except for the top piston. Tests were performed on individual sand samples (7.5 g in mass), taken from each of the three sieved fractions, at room temperature, under both dry and drained, wet conditions. Each sand sample was deposited into the open vessel using an elongated glass funnel to prevent grains from sticking to the vessel wall. In all cases, the sample was surrounded by a thin-walled Teflon sleeve or pot (height 16 mm, thickness  $0.13 \pm 0.02$  mm) previously inserted into the bore of the vessel to reduce friction between the sample and the vessel wall. After introduction of the sample, the top piston was inserted into the vessel until the sample was just touched, and the assembly was mounted into the Instron apparatus. The top piston was withdrawn by 1–2 mm, and the vessel was tapped with a mallet to settle the sample and thus obtaining a near-constant sample length. The piston was then gently advanced in “position control” mode until a small set point stress equal to 0.24 MPa was achieved. At this stage, the system was switched into “load control” mode. The initial sample length (~16 mm) was determined using the Instron LVDT as a measure of piston position and using a pair of vernier calipers (50  $\mu\text{m}$  precision) to measure protrusion of the top piston from the vessel [cf. Brzesowsky *et al.*, 2014]. Since the diameter of the vessel bore is 20 mm, the radius of the sample was taken as 9.9 mm when calculating the initial porosity, at the set point load, and the applied stress during the test. Note that porosity was calculated using the stated sample dimensions and sample mass, assuming a density for quartz of  $2.648 \text{ g/cm}^3$ . Overall, the setup procedure produced a well-controlled starting aggregate with a reproducible porosity of  $42 \pm 0.3\%$ . The initial agitation and minor loading of the sand was intended to produce a more or less locked aggregate aimed to diminish the role of pure interparticulate settling in accommodating compaction during loading. After determining their initial lengths, the samples were subjected to either two-stage or single-stage creep tests, as described above. Overall, 37 successful tests were performed with the various experimental variables and under the conditions listed in Table 1 (two-stage creep tests) and Table 2 (single-stage creep tests).

The three different “dry” states investigated are referred to as “lab-dry” (in equilibrium with lab air), “evacuated,” and “vacuum-dried” conditions. The evacuated condition was achieved by simply attaching a

**Table 2.** Overview of the Single-Stage Creep Tests Performed on Sands at Room Temperature Under Flooded Conditions<sup>a</sup>

Expt.	$\sigma_a$ (MPa)	$d$ ( $\mu\text{m}$ )	$\phi_i$ (%)	Condition	Time (days)
BS37, BS40, and BS41	30	275 $\pm$ 25	37.4; 37.4; 37.6	aq. solution	7; 3; 7
BS38 and BS39	30	275 $\pm$ 25	37.8; 37.7	<i>n</i> -decane	7
BS43	20	275 $\pm$ 25	39.4	aq. solution	7
BS42	10	275 $\pm$ 25	40.7	aq. solution	5

<sup>a</sup>Symbols:  $\sigma_a$  is the applied stress (MPa),  $d$  is grain size ( $\mu\text{s}$ ),  $\phi_i$  is the porosity at the start of the creep stage (%).

vacuum hose line to the pore fluid in/outlet in the top piston (see Figure 2) after initial loading at 0.24 MPa, followed by evacuation using a single-stage rotary vacuum pump. This is assumed to have resulted in partial drying with respect to the lab-dry condition. For the vacuum-dried tests, the vacuum pump was connected to the pore fluid inlet via a Drechsel bottle, filled with silicone oil, and then two glass chambers filled with activated alumina or phosphorous pentoxide ( $\text{P}_2\text{O}_5$ ) as a drying agent (system vapor pressure:  $< 0.7$  kPa). The latter was done to ensure that the vacuum-dried system would be devoid of any water vapor. Drained, wet (pore fluid pressure  $P_p = 1$  atm) test conditions were achieved by vacuum flooding the sample, either after dry creep (two-stage creep tests) or at the initial set point stress (single-stage creep tests), with an inert fluid (*n*-decane, analytical grade  $\text{C}_{10}\text{H}_{22}$ ), with distilled water saturated with silica, or with an NaCl solution (1 or 6.15 M NaCl) saturated with silica.

Tests were terminated by unloading the samples to the initial set point stress (0.24 MPa) at a constant rate in the range 282–550 MPa/h. Wet samples were then briefly evacuated to remove the bulk of the pore fluid phase, allowing air to enter via the air inlet in the vessel wall (Figure 2). After reducing the load to zero, the apparatus was taken out of the testing rig and the top piston was removed. Subsequently, while pressing a glass piston (external diameter = 20 mm) gently against the top of the sample to hold it in place, the vessel was turned upside down and the upper segment of the bottom piston was removed. Each sample was then carefully extracted from the vessel and placed in a cylindrical polyfine container. Wet samples were then dried for 2–3 days at  $\sim 70^\circ\text{C}$  in a drying oven. In this way, minimum disturbance to the friable sample structure was achieved. Prior to thin sectioning, samples were impregnated with blue-colored epoxy resin. Not all dry samples could be retrieved due to their loose nature. One sample (BS10), tested using a Teflon pot (i.e., sleeve closed at bottom end), was impregnated with epoxy resin before removal from the vessel. A second (BS44) was flooded with *n*-decane at the set point load to enhance its cohesion. It should be noted that microstructural analysis showed that the typical removal of the sample, by gently pressing it out, did not notably disturb the sample, compared to BS10 and BS44. No special precautions were taken to preserve the coherence of the remaining dry-tested samples (BS2 and BS7), which were removed dry, in disturbed condition. At the end of each sand compaction test, the Teflon sleeves or pot were found to be intact, i.e., not perforated by the sand grains, and of more or less unchanged thickness.

#### 2.4. Data Acquisition/Logging

During the experiments, axial load, Instron LVDT position, Sangamo LVDT position, and temperature were logged at various time intervals of 5 to 600 s, depending on the creep rate. In addition, the cumulative number of acoustic emission events was logged by a separate system using the same time base. The Sangamo LVDT displacement and raw Instron load data were used to construct volumetric strain versus applied axial stress plots. The displacement data were corrected for elastic distortion of the apparatus using predefined, tenth-order polynomial stiffness calibrations. Except where otherwise mentioned, instantaneous volumetric strain  $e_v$  was calculated with respect to the length of the sample at the beginning of the dry and wet creep stages respectively, i.e., defining a strain origin at the start of each creep or constant stress stage. Instantaneous volumetric strain was calculated directly from the displacement versus time records obtained for each experiment in terms of the engineering strain, defined as  $e_v = -\Delta V/V_0$ , which for our uniaxial compaction experiments is equal to  $e_v = -\Delta L/L_0$ . Instantaneous strain rates, defined as  $\dot{\epsilon} = -(1/L)(dL/dt)$ , were calculated by performing linear regression fits to the corrected displacement versus time data, using a moving displacement interval chosen such that the maximum error in compaction rate was always less than  $\pm 5\%$ . Conventional error analysis showed the absolute or relative errors in both logged and processed values

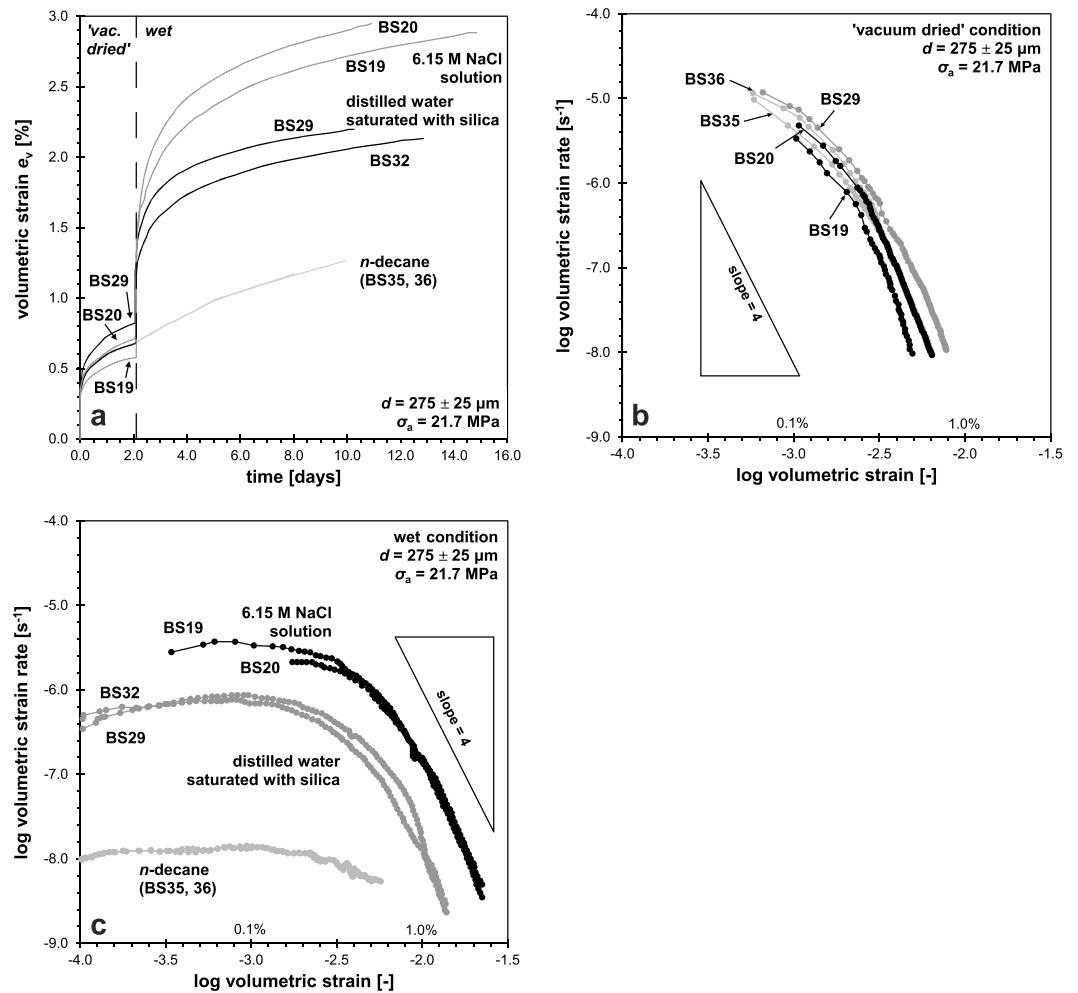


**Figure 3.** Two-stage compaction creep experiments performed on sands of the  $275 \pm 25 \mu\text{m}$  grain size  $d$  fraction, at room temperature, at a constant applied stress  $\sigma_a$  of 21.7 MPa, and under vacuum-dried and subsequent wet conditions. (a) Volumetric strain versus time plot, (b) log volumetric strain rate versus log volumetric strain plot for the dry stage, and (c) for the wet stage.

of Instron load, Instron displacement, Sangamo LVDT displacement, applied axial stress, and volumetric strain to be less than 0.3%, 0.3%,  $5 \mu\text{m}$ , 0.5%, and 0.6%, respectively. As these errors are smaller than the symbol size, no attempt has been made to plot error bars for individual points in our graphs. The acoustic emission event counting was used to calculate the instantaneous AE event rate from the change in cumulative events occurring in the same time window as used for the strain rate calculations.

### 3. Mechanical Data

#### 3.1. Two-Stage Creep Experiments

Two-stage compaction creep curves illustrating the effect of chemical environment are shown in Figure 3a. The data were obtained from tests performed on sand from the  $275 \pm 25 \mu\text{m}$  size fraction, at a constant applied stress of 21.7 MPa, and under vacuum-dried and subsequent wet conditions. The volumetric strain data displayed in Figure 3a were calculated with respect to the length of the sample at the beginning of the vacuum-dried creep stage. Furthermore, the discrete data were used to construct plots of volumetric strain rate ( $\dot{\epsilon}$ ) versus volumetric strain ( $e_v$ )—see Figures 3b and 3c.

From Figures 3a and 3b, it is evident that samples maintained in the vacuum-dried condition exhibited strongly decelerating creep falling to rates of  $\sim 10^{-8} \text{ s}^{-1}$  after approximately 2 days. However, Figures 3a and 3c

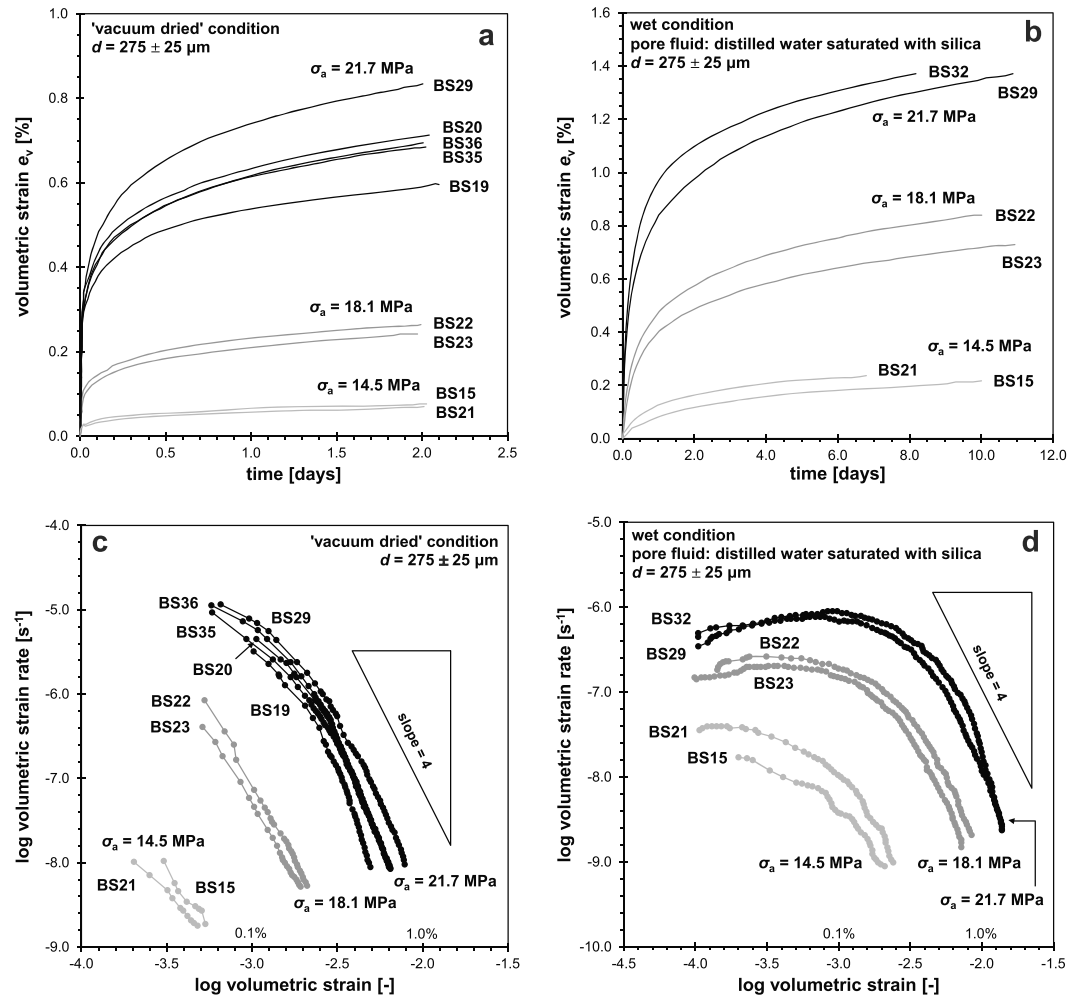


**Figure 4.** Two-stage compaction creep experiments performed at  $\sigma_a = 14.5\text{--}21.7$  MPa. Volumetric strain versus time plots are shown for (a) the vacuum-dried stage and (b) the wet stage. Log volumetric strain rate versus log volumetric strain plots are also shown for (c) the vacuum-dried stage and (d) the wet stage. The creep data obtained from test BS32 were affected by room temperature drift and are hence excluded.

illustrate that the later addition of aqueous pore fluids resulted in a dramatic enhancement of creep, with creep being particularly favored by an increased pore fluid salinity (NaCl content). In contrast, flooding with inert pore fluid (*n*-decane) showed only slightly enhanced creep rates. In all cases, no instantaneous deformation was observed at the point of flooding. Two-stage creep tests performed on the same material at 30.0 MPa, and under evacuated or vacuum-dried and subsequent wet conditions, showed closely similar effects of chemical environment (not presented). Again, the addition of aqueous pore fluids accelerated creep dramatically, with creep being enhanced by an increased pore fluid salinity. On the other hand, no systematic effect of vacuum condition (evacuated versus vacuum dried) was observed.

Two-stage compaction creep curves and  $\dot{\epsilon}$  versus  $e_v$  plots, obtained from two-stage creep tests, reflecting the effect of applied stress ( $\sigma_a$ ) on creep under vacuum-dried and wet conditions are depicted in Figure 4. Similar plots, visualizing the effect of grain size ( $d$ ) on creep, are shown in Figure 5. Clearly, creep was favored and compaction rates (at constant  $e_v$ ) increased with increasing  $\sigma_a$  and  $d$ . Note that the effect of  $\sigma_a$  and  $d$  on creep behavior was similar for vacuum-dried and wet samples.

Overall, creep was favored and compaction rates (measured at constant  $e_v$ ) were enhanced with increasing  $\sigma_a$ . However, the effect of  $d$  was less clear-cut, with the intermediate grain size exhibiting faster creep in the first 8 days than either the coarse or fine fractions. Assuming a power law relation between the strain rate

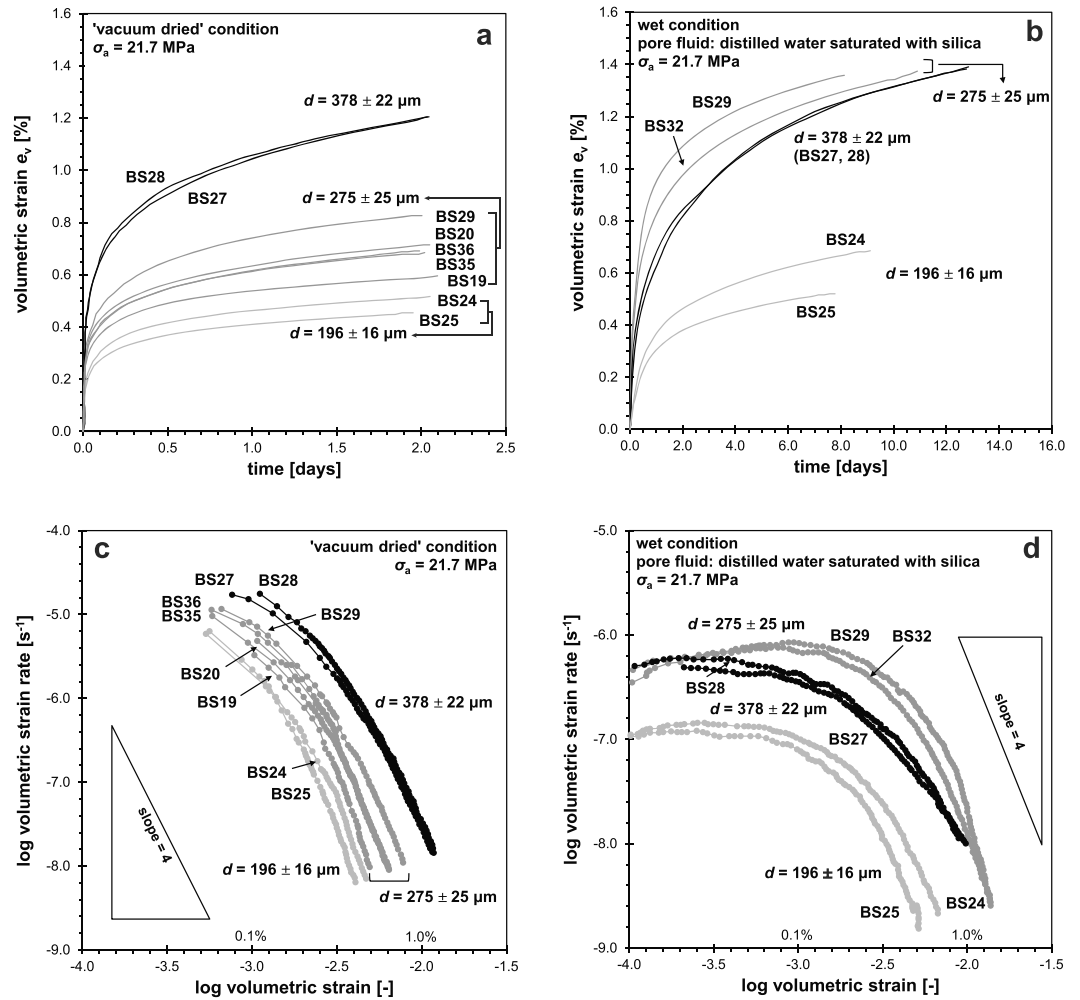


**Figure 5.** Two-stage compaction creep experiments performed on sands of different grain size ( $d = 196 \pm 16 \mu\text{m}$ ,  $275 \pm 25 \mu\text{m}$ , and  $378 \pm 22 \mu\text{m}$ ). Volumetric strain versus time plots are shown for (a) the vacuum-dried stage and (b) the wet stage. Log volumetric strain rate versus log volumetric strain plots are shown for (c) the vacuum-dried stage and (d) the wet stage. The creep data obtained from test BS32 were excluded due to room temperature drift affecting the measurements.

and applied stress, i.e.,  $\dot{\epsilon}_v \propto \sigma_a^f$ , the data depicted in Figures 4c and 4d imply the exponent  $f$  to be  $\sim 21$  under vacuum-dried conditions ( $e_v = 0.05\%$ ) and  $\sim 12\text{--}17$  under wet conditions ( $e_v = 0.1\text{--}0.25\%$ ) demonstrating extreme sensitivity of  $\dot{\epsilon}_v$  to  $\sigma_a$ . With regard to the sensitivity of strain rate to  $d$ , i.e., assuming  $\dot{\epsilon}_v \propto d^g$ , the data shown in Figures 5c and 5d yield an exponent  $g$  of  $\sim 4\text{--}8$  under vacuum-dried conditions ( $e_v = 0.1\text{--}0.5\%$ ) and  $\sim 6\text{--}11$  under wet conditions ( $e_v = 0.01\text{--}0.5\%$ ,  $d = 196 \pm 16$  and  $275 \pm 25 \mu\text{m}$ ). The  $\dot{\epsilon}_v$  versus  $e_v$  plots depicted in Figures 3b and 3c, 4c and 4d, and 5c and 5d demonstrate compaction creep rates of sands under vacuum-dried and wet (aqueous pore fluids) conditions to hardly differ at similar  $e_v$  ( $> 0.5\%$ ),  $\sigma_a$  and  $d$ , and to be roughly proportional to  $e_v^{-4}$ . The creep data obtained from two-stage creep tests performed at 20.0 and 30.0 MPa, using distilled water saturated with silica as pore fluid (BS13 and BS7, respectively), are omitted from Figures 4 and 5 due to a different initial loading procedure, resulting in a different starting porosity (cf. Table 1). Moreover, at applied stresses of 7.2 and 10.9 MPa, neither the dry nor wet samples, where the pore fluid was distilled water saturated with silica, exhibited creep. Therefore, these corresponding creep data are also excluded from Figures 4 and 5 (BS16 to BS18—see Table 1).

### 3.2. Single-Stage Creep Experiments

Compaction creep curves and  $e_v$  plots illustrating the effect of chemical environment on the creep of samples tested in single-stage mode are shown in Figure 6. All data presented were obtained from tests performed on

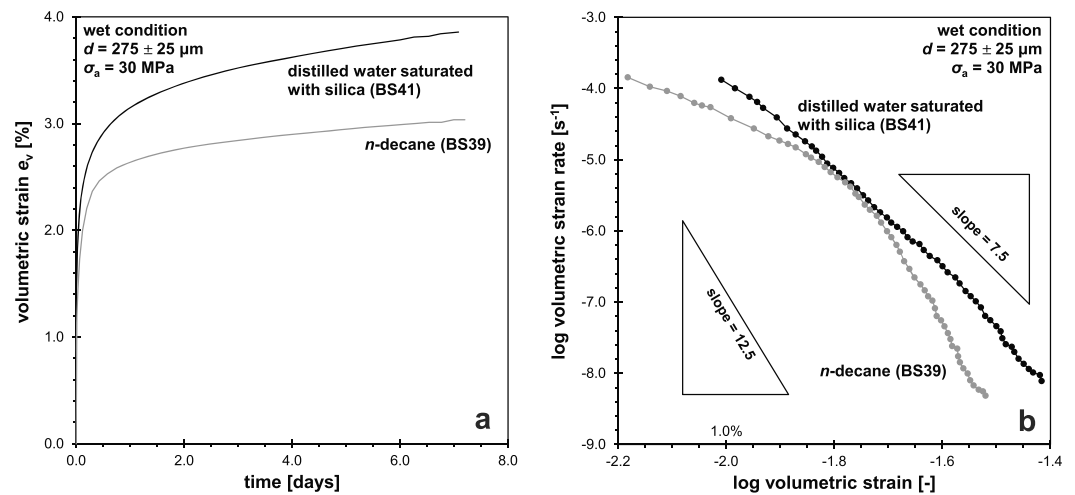


**Figure 6.** (a) Volumetric strain versus time and (b) log volumetric strain rate versus log volumetric strain plots obtained from single-stage creep tests performed on sands of the  $275 \pm 25 \mu\text{m}$  grain size fraction, at a constant applied stress  $\sigma_a$  of 30 MPa, under wet conditions.

material from the  $275 \pm 25 \mu\text{m}$  size fraction, at an applied stress of 30.0 MPa under wet conditions. Since the reproducibility of the creep data is highly sensitive to the starting porosity, only data of tests BS39 and BS41, having similar starting porosities, are displayed (cf. Table 1). The volumetric strain ( $e_v$ ) data displayed in Figure 6 were calculated with respect to the length of the sample at the point when load ramping was stopped, i.e.,  $e_v$  does not include ramping strain. At  $e_v > 1.6\%$ , more creep and faster creep rates were obtained in the sample flooded with distilled water saturated with silica, in comparison to the sample flooded with *n*-decane. Similar graphs showing the effect of applied stress ( $\sigma_a$ ) on creep under conditions where the pore fluid was distilled water saturated with silica are depicted in Figure 7. Evidently, initial compaction (creep) and creep rates (at constant  $e_v$ ) strongly increased with increasing  $\sigma_a$ . Assuming a power law relation  $\dot{\epsilon} \propto \sigma_a^f$ , the data displayed in Figure 7 imply the exponent  $f$  to be  $\sim 15$  under wet conditions ( $e_v = 0.8\%$ ). At  $e_v > 1.6\%$ , Figure 6b and 7b show that compaction rates in the single-stage creep tests (at constant strain) are roughly proportional to  $e_v^{-7.5}$ , in case of samples flooded with distilled water saturated with silica, and to  $e_v^{-12.5}$ , in case of samples flooded with *n*-decane.

#### 4. Acoustic Emission Data

Acoustic emission (AE) data were obtained during both the two-stage creep tests (BS27–BS36 and BS44—see Table 1) and the single-stage compaction creep experiments BS37 to BS43 (Table 2).

##### 4.1. Two-Stage Creep Tests

Cumulative AE event count versus  $e_v$  data representative of two-stage creep tests (BS32 and 36) performed on  $275 \pm 25 \mu\text{m}$  sand samples, at an applied stress of 21.7 MPa, are shown in Figure 8. These data show a near-linear relation between  $e_v$  and cumulative AE event counts, as well as a clear effect of chemical environment on acoustic emission activity. Note that overall, the data are not significantly affected by the pulse stretching time (PST). After the addition of pore fluid, the number of AE event counts, obtained per unit  $e_v$ , shows a significant increase in comparison with the vacuum-dried stage. Furthermore, the samples flooded with distilled water saturated with silica yielded slightly more AE event counts per  $e_v$  than material flooded with *n*-decane. Since different settings of the AE system (and a different initial loading procedure) were employed during creep tests at 30.0 MPa, the effect of applied stress on AE activity could not be assessed (cf. section 2).

The cumulative AE event counts depicted in Figure 8a were used to construct the plot of AE event count rate (average rate for current logging interval) versus  $e_v$  displayed in Figure 8b. This clearly illustrates that the addition of pore fluid resulted in a large increase in the time rate of AE event counts and that count rates at constant  $e_v$  were higher in samples flooded with aqueous solution than with *n*-decane.

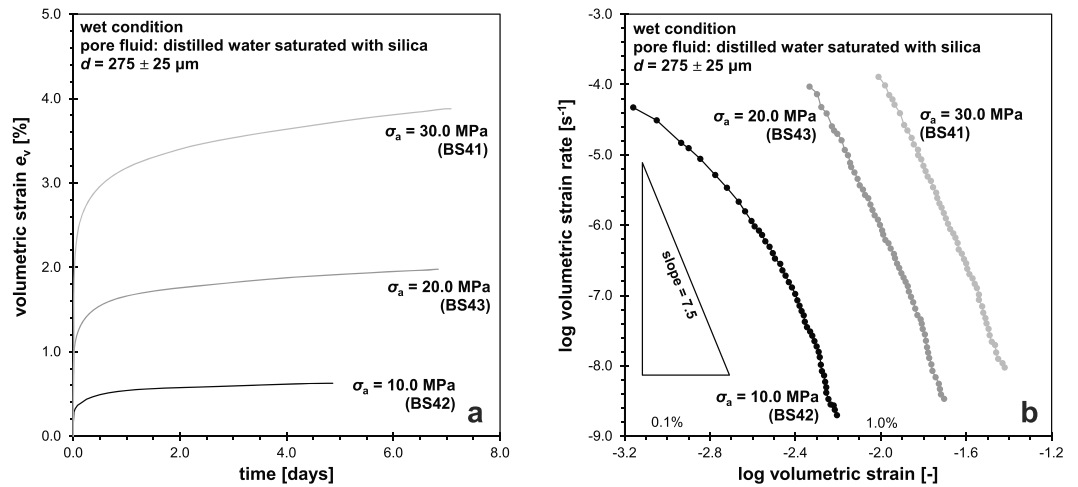


**Figure 7.** (a) Volumetric strain versus time and (b) log volumetric strain rate versus log volumetric strain plots obtained from single-stage creep tests performed on sands of the  $275 \pm 25 \mu m$  grain size fraction under wet conditions, reflecting the effect of applied stress  $\sigma_a$ .

Similar plots illustrating the effect of grain size on AE characteristics in two-stage creep tests, performed at 21.7 MPa, are presented in Figure 9. The data again show a near-linear relation between cumulative AE event counts and  $e_v$ . Moreover, the data demonstrate that during both the vacuum-dried and the flooded creep stages, the coarser-grained samples yielded fewer AE event counts per unit  $e_v$  than the finer ones. At constant  $e_v$ , however, the data displayed in Figure 9b show a trend toward higher AE event count rates with increasing grain size. It is important to realize here that the AE event rate and strain accumulated per grain is much less in the fine-grained than in the coarser-grained samples so that more creep strain is accumulated in the coarser-grained samples, meaning they are “weaker” [see also Brzesowsky *et al.*, 2014].

**4.2. Single-Stage Creep Tests**

Representative cumulative AE event count and AE event count rate data obtained from the single-stage creep tests ( $d = 275 \pm 25 \mu m$ ,  $\sigma_a = 10.0\text{--}30.0$  MPa) are shown in Figure 10. During initial stages of creep, the data depicted in Figure 10a exhibit a highly nonlinear relation between cumulative AE event counts and  $e_v$  which intensifies with increasing applied stress. At strains of more than 1.5%, the data show a near-linear

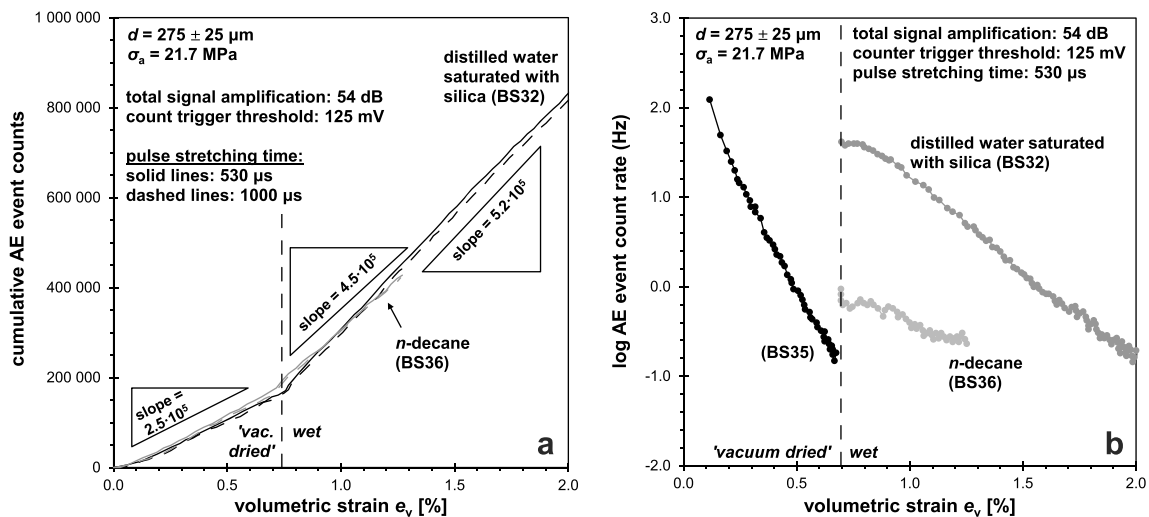


**Figure 8.** (a) Cumulative AE event count versus volumetric strain data obtained during typical two-stage creep tests (BS32 and BS36) performed on sands of the  $275 \pm 25 \mu m$  grain size fraction, at a constant applied stress of 21.7 MPa. (b) Plot of AE event count rate versus volumetric strain constructed using the cumulative AE event count data for BS32 and BS36, as presented in Figure 8a.

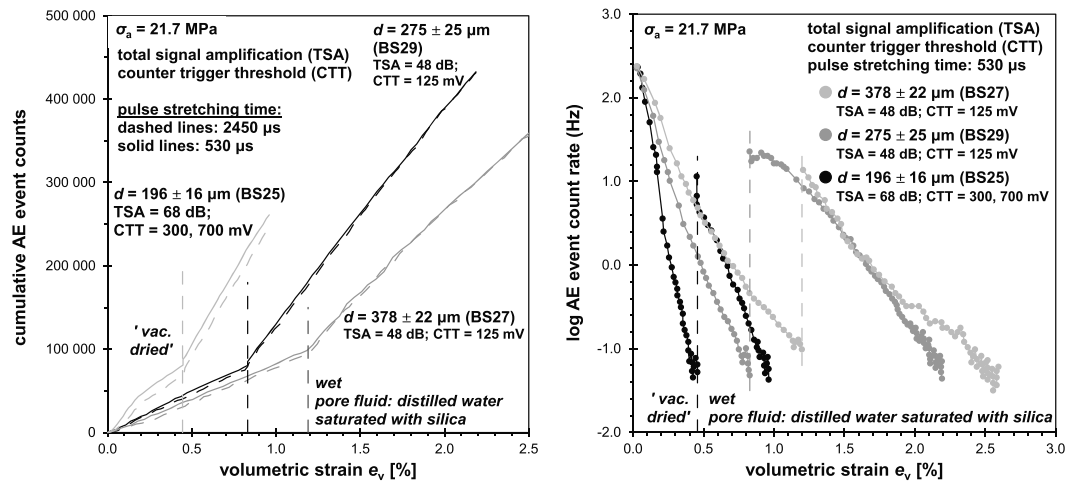


**Figure 9.** (a) Cumulative AE event count and (b) AE event count rate versus volumetric strain obtained during typical two-stage creep tests (BS25, BS27, and BS29) showing the effect of grain size, at an applied stress of 21.7 MPa.

relation between cumulative AE event counts and  $e_v$  as well as clear effects of  $\sigma_a$  and chemical environment. Note that slightly more AE events are counted at a higher PST. With increasing  $\sigma_a$ , a larger number of AE event counts is obtained both per unit  $e_v$  and at constant  $e_v$ , with a PST of 530  $\mu\text{s}$ . Furthermore, the samples tested at 30.0 MPa and flooded with distilled water saturated with silica yielded more AE event counts at constant  $e_v$  than material flooded with *n*-decane. At constant  $e_v$ , the data presented in Figure 10b show that AE event count rates were significantly higher with increasing  $\sigma_a$  and higher in sands tested at 30.0 MPa and flooded with distilled water saturated with silica, in comparison to material drained in *n*-decane.

The nonlinear relation between cumulative AE event count and  $e_v$  obtained during the initial stages of creep illustrates the inability of the AE signal conditioning system to “count” AE event rates above 1300 Hz. In general, during all creep tests, minor undercounting of AE events, due to, e.g., clustering of AE events in time, cannot be ruled out so that AE event count (rate) data should be regarded a lower bound of the actual AE event rate.

### 5. Microstructural Observations

Microstructural analysis was performed on thin sections of the deformed sand samples using transmitted light optical microscopy. Thin sections of the impregnated sand samples were prepared from perpendicular slices cut parallel to the sample axis. Representative micrographs of the microstructures are shown in Figure 11.

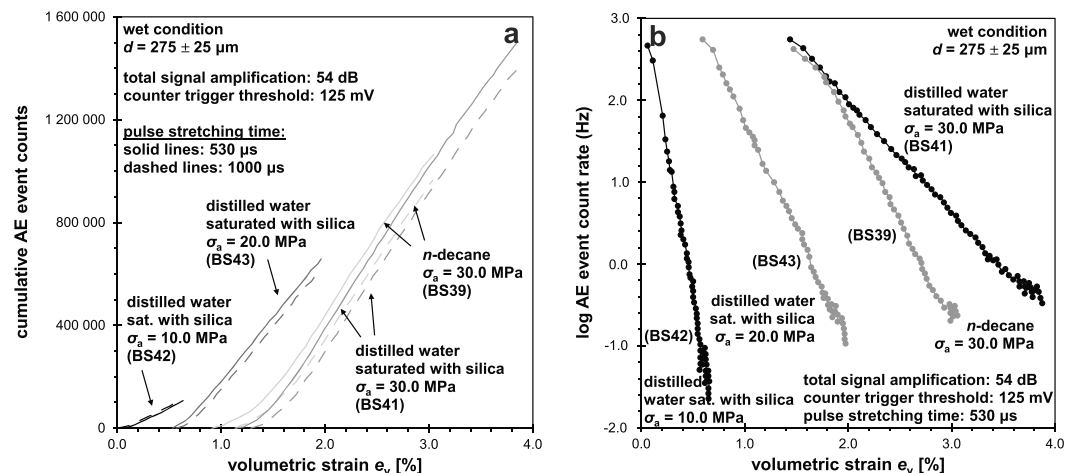


**Figure 10.** (a) Cumulative AE event count and (b) AE event count rate versus volumetric strain obtained during typical single-stage creep tests (BS39 and BS41–BS43) performed on sands of the 275  $\pm$  25  $\mu\text{m}$  grain size fraction under wet conditions.

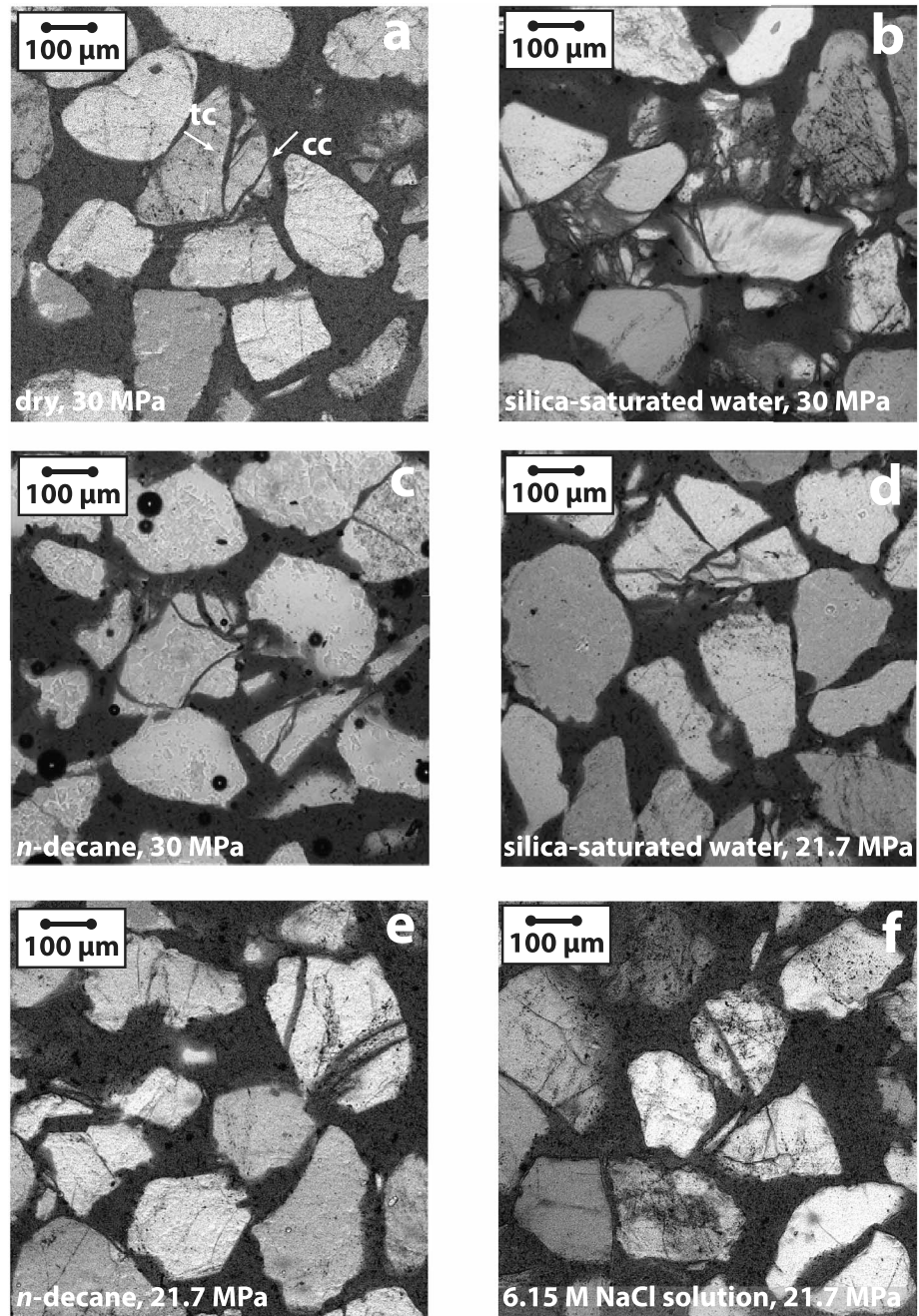


**Figure 11.** Micrographs of sand samples subjected to creep under different conditions at room temperature. (a) Sample BS44 subjected to creep under “vacuum-dry” conditions during the first phase of a two-stage creep test. Note the transgranular (tc) and divergent cone cracks (cc) fanning out from grain-to-grain contacts. (b) Sample BS31 subjected to second-stage creep under wet conditions. The microstructure exhibits intense grain fragmentation, with clusters of ~10–25 cracks per failed grain radiating from grain-to-grain contacts. (c) Sample BS39 subjected to single-stage creep under wet conditions. The microstructure is closely similar to that seen in Figure 11a, except that a smaller fraction of grains are broken. (d) Sample BS32 subjected to second-stage creep under wet conditions at a lower applied stress than Figure 11b. The microstructure looks similar to that of Figure 11b, exhibiting grains fragmented due to multiple, transgranular, and divergent cone cracks fanning out from grain-to-grain contacts. (e) Sample BS35 subjected to second-stage creep under wet conditions. The microstructure is similar to that of Figure 11a, but fewer grains have failed due to a lower applied stress. (f) Sample BS20 after a two-stage creep test under wet conditions, showing clusters of three to eight cracks per failed grain.

Description of the microstructures will focus on the effect of chemical environment (dry versus wet, pore fluid composition), grain size, and applied stress. We focus on microstructures obtained under the extreme conditions, i.e., vacuum dried versus wet at an applied stress of 21.7 or 30.0 MPa, representing end-member microstructure signatures. Moreover, the microstructures observed in sands from the  $275 \pm 25 \mu\text{m}$  fraction, subjected to two-stage or single-stage creep under wet conditions at applied stresses lower than 21.7 MPa, were found to contain similar features as samples subjected to creep under wet conditions at an applied stress of more than 21.7 MPa, although the amount of microstructural damage accumulated was lower.

The undeformed quartz sand showed well-rounded grains and narrow grain size distributions. After deformation, all compacted samples showed evidence of cone cracks occurring within grains (intragranular cracks) and cross-cutting grains (transgranular cracks). Cone cracking is characterized by divergent ("spalling") and convergent ("onion peel") cracks, fanning out from grain-to-grain contacts. In general, we note that no obvious unloading features (horizontal cracks) or compaction band features were apparent in the samples. In our microstructural analyses, crack density is defined as the mean number of cracks per grain. Both crack density and the fraction of failed grains  $F_{\text{bg}}$  were obtained by point counting of over 500 grains, using the line interception method applied to representative thin sections. It should be noted that our approach to measuring crack density is very similar to the normalized linear crack density (NLCD) method as described by *Bauer and Johnson* [1979], which defines NLCD as the number of cracks normalized with respect to the number of grain boundaries. For porous materials, as used in our experiments, our method varies by roughly a factor of 2 compared to theirs.

Sand grains deformed under vacuum-dried conditions at an applied stress of 30.0 MPa (BS10 and BS44), during the first phase of a two-stage creep test, showed ~30% grain failure, exhibiting transgranular and divergent cone (spalling) cracks fanning out from crushed, grain-to-grain contacts (Figure 11a). These cracks (~1–3 per failed grain) are generally straight, cut the preexisting closed cracks or inclusion trails observed in the undeformed sands, and do not widen to such an extent that the grains lose cohesion.

In contrast, samples subjected to second-stage creep under wet conditions, using an aqueous pore fluid, exhibit far more transgranular and divergent cone cracks fanning out from grain-to-grain contacts. The grains are fragmented due to multiple, generally curved cracks, resulting in high angularity and broken-off grain fragments. After flooding (distilled water saturated with silica), sand loaded at an applied stress of 30.0 MPa (BS31;  $e_v = 8.9\%$ ), ~90% of the grains have failed and show intense grain fragmentation, with clusters of ~10–25 cracks per failed grain radiating from grain-to-grain contacts (see Figure 11b).

Sand subjected to single-stage creep under the same conditions (BS41:  $\sigma_a = 30.0$  MPa; distilled water saturated with silica) shows deformation features broadly corresponding to the microstructural damage of sands subjected to two-stage creep at 30.0 MPa using similar pore fluid: ~80% of the grains have failed with 5–15 cracks per failed grain. On the other hand, sand subjected to single-stage creep at 30.0 MPa using *n*-decane as pore fluid (BS39) shows only approximately 40% grain failure with one to four cracks per failed grain (Figure 11c).

At lower applied stress ( $\sigma_a = 21.7$  MPa), samples loaded under otherwise similar conditions (BS32:  $e_v = 4.6\%$ , distilled water saturated with silica) show evidence that roughly 50% of the grains have failed, exhibiting ~2–5 cracks per failed grain (see Figure 11d). On the other hand, the deformation microstructure observed in material loaded at 21.7 MPa and flooded with an inert fluid like *n*-decane (BS35; Figure 11e) is closely similar to the microstructure of dry deformed material, except that only ~20% of the grains have failed. In material loaded to the same stress but flooded with a 6.15 M NaCl solution saturated with silica (BS19 and BS20; Figure 11f), more grains show grain failure (~60%) and exhibit ~3–8 cracks per failed grain. Sands taken from the three different grain size fractions (BS24, BS32, and BS28:  $\sigma_a = 21.7$  MPa; distilled water saturated with silica) typically show a closely similar deformation microstructure. However, the microstructural damage accumulated, i.e., the fraction of failed grains, increases slightly with larger grain size.

In summary, the microstructural observations show a significant effect of chemical environment, with sand samples subjected to two-stage creep and flooded with an aqueous (chemically active) pore fluid showing a substantially larger fraction of failed grains and far more cracks per grain in comparison with material subjected to only the first vacuum-dried phase of the test, or to single-stage creep and flooded with an inert fluid (*n*-decane). Furthermore, the fraction of grain failure increases with higher NaCl concentration. Under

wet conditions, the samples also showed an increase in the fraction of broken grains and the number of cracks per grain with higher applied stress and, to a lesser extent, with increasing grain size.

## 6. Discussion: The Mechanism of Compaction Creep

The mechanical data presented above demonstrate that the compaction behavior of the dry and wet sand aggregates is time dependent. Moreover, the relatively insignificant effect of flooding dry samples with *n*-decane suggests that pure frictional compaction processes, i.e., particle sliding with no chemical effects, played a minor role during the vacuum-dried and wet phases of the two-stage creep tests, implying that the samples reached a “locked” aggregate state during the initial load ramping/cycling stage. After “locking” of an aggregate, further compaction can be achieved through deformation of the grains and grain-to-grain contacts. This is in accordance with microstructural observations made on sand samples subjected to either two-stage creep under dry and subsequent wet conditions or to single-stage creep under wet conditions, which show particle crushing caused by time-dependent transgranular and divergent cone cracking under dry and wet conditions. We continue to discuss the potential mechanisms behind the effect of chemical environment, as well as the influence of grain size and applied stress on the observed volumetric strain behavior.

### 6.1. The Effect of Chemical Environment on Compaction Creep

The observed enhancement of creep and microcracking by an added aqueous pore fluid suggests the promotion of creep by chemically related brittle deformation processes of the sand grains/contacts, such as subcritical crack growth. In the presence of aqueous fluids, subcritical growth of cracks in quartz is classically explained in terms of “stress corrosion cracking” [Atkinson, 1979; Atkinson and Meredith, 1981; Dunning *et al.*, 1994; Fisk and Michalske, 1985; Michalske and Bunker, 1987]. Overall, this process is controlled by  $H^+$ ,  $H_2O$ , and  $OH^-$  adsorption onto quartz surface groups ( $\equiv Si-OH$ ) and by hydrolysis of siloxane ( $\equiv Si-O-Si \equiv$ ) bonds [Charles, 1958; Dove, 1995; Michalske and Freiman, 1982; Xiao and Lasaga, 1994], leading to weakening of strained Si-O bonds at crack tips, followed by bond rupturing.

The observed effect of pore fluid salinity on creep (cf. Figure 3) suggests that increasing NaCl concentration in solution promotes the brittle deformation processes in the sand grains and at grain contacts, e.g., by lowering the activation energy for stress corrosion crack growth and therefore speeding up its kinetics. This is in accordance with experiments performed on quartz and soda-lime glass, which showed that surface complexation of  $Na^+$  with  $\equiv Si-O^-$  surface groups to form  $\equiv Si-O-Na$  resulted in the opening and stretching of  $\equiv Si-O-Na$  bonds, making them more prone to  $H_2O$  attack [Charles, 1958; Dove and Elston, 1992; Hangx *et al.*, 2010; Wiederhorn and Bolz, 1970]. This effect has been supported by theoretical predictions made by Hiemstra and van Riemsdijk [1990]. Furthermore, the  $Na^+$  ions are considered to enhance the local dissociation of water, providing  $OH^-$  ions for attack of the Si atoms and leading to rupture of adjacent Si-O bonds [Dove, 1994; Dove and Elston, 1992; Gratz and Bird, 1993a, 1993b].

The effect of chemical environment on creep is supported by the observed acoustic emission (AE) activity. A control experiment showed no acoustic emission (AE) activity during loading of a steel dummy sample. Moreover, it is unlikely that any AE activity would have been detected during long-term loading of the dummy sample at constant stress. Consequently, the AE events observed during sand compaction creep under both dry and wet conditions are inferred to be caused by the sample, i.e., by time-dependent grain crushing involving transgranular and divergent cone cracking and by sliding-induced rearrangement of grains and grain fragments.

The near-linear relation between cumulative AE event count and  $e_v$ , obtained during two-stage and single-stage creep tests, under dry and wet conditions, suggests that each grain failure event contributed to a more or less constant amount of volumetric strain [see also Brantut *et al.*, 2013, Figure 15]. Therefore, the larger number of AE events counted per unit  $e_v$  during the wet phase of a two-stage creep test using distilled water saturated with silica as pore fluid, in comparison with such data obtained during the vacuum-dried stage or during the final phase with samples drained in *n*-decane, may be explained by the larger number of cracks per grain observed in the microstructure, which is in accordance with a fluid-assisted deformation mechanism. The linear relationship between AE number and strain observed here in sand is also consistent with similar observations made on sandstones during time-dependent, brittle creep experiments

[e.g., Heap *et al.*, 2009]. This similarity implies that the process of deformation by time-dependent grain failure and subsequent microstructural rearrangement might be a shared feature in both cemented and uncemented porous rocks.

## 6.2. Effects of Grain Size and Applied Stress on Compaction Creep—Evidence From Acoustic Emissions

A rough, positive dependence on grain size is observed during the wet phase of the two-stage creep tests performed on sands from the three different size fractions (cf. Figure 5). This is inferred to be due to the larger amount of volumetric strain accumulated by the largest grain size fraction during the vacuum-dried creep phase, leading to a relatively larger grain size reduction than other, smaller, size fractions, and hence giving rise to slower creep during the wet phase.

However, a clear effect of grain size on the number of AE events ( $n_{AE}$ ) counted per unit  $e_v$  can be seen (Figure 9). This behavior may be explained with a simple model in which failure of a sand grain is considered to contribute to an incremental volume change equal to  $\alpha d^3$ , where  $\alpha$  is a dimensionless constant ( $0 \leq \alpha \leq \pi/6$ ). Accordingly, the inelastic volumetric strain  $e_v^{in}$  accumulated due to failure of a cumulative number  $n_N$  of grains is defined by the relation  $e_v^{in} = (n_N \alpha d^3)/V_0$ , where  $V_0$  is the initial (bulk) volume of the sand sample. It is further assumed that  $n_{AE}$  and  $n_N$  are linearly related through the relation  $n_{AE} = B(\sigma_a, d) n_N$ , where  $B(\sigma_a, d)$  is the number of AE events per failing grain, equal to the number of incremental crack surface steps and hence proportional to the total crack surface created [e.g., Lysak, 1994], and that the crack surface created scales with  $d^2$  so that  $B(\sigma_a, d) = C(\sigma_a) d^2$ , where  $C$  being a function of the applied stress  $\sigma_a$ . Accordingly, it is easily shown that the number of AE events counted per unit  $e_v^{in}$  is expressed as  $dn_{AE}/de_v^{in} = C(\sigma_a)V_0/(\alpha d)$ . The cumulative AE event counts depicted in Figure 8a suggest that the number of AE events counted per unit  $e_v$  is roughly proportional to  $d^{-0.9}$  which is in close agreement with the model.

Moreover, the cumulative AE event counts depicted in Figure 8a, from samples flooded with aqueous pore fluid, suggest that the number of AE events counted per unit  $e_v$  is roughly proportional to  $\sigma_a^{0.9}$ . Consequently, a possible explanation for the observed stress dependence of the AE data might be that  $C(\sigma_a)$  is a linear function of  $\sigma_a$  (since  $\alpha$  is likely to be independent of  $\sigma_a$ , as shown in Brzesowsky *et al.* [2014]). This may be a reasonable suggestion, since the microstructural observations have shown that the number of cracks per failed grain increases with increasing  $\sigma_a$ .

In summary, combining the interpretations of the mechanical, microstructural, and AE data discussed above, it is inferred that the compaction creep behavior of the sand aggregates under both dry and wet conditions is primarily controlled by time-dependent contact cracking leading to crushing of grains. This time-dependent grain failure process is clearly promoted by a chemically active pore fluid, by a higher pore fluid salinity, by a larger grain size, and by a higher applied stress. Although the detailed time-dependent cracking mechanisms are unknown, it is likely that crack growth by stress corrosion is predominantly operative in the presence of aqueous solutions.

## 7. Microphysical Modeling of Time-Dependent Brittle Deformation of Sand Aggregates

As stated previously, in our experiments, compaction creep at constant applied stress is caused by brittle deformation due to time-dependent failure of individual grains, which is likely due to stress corrosion cracking [Atkinson, 1979]. As such, grain failure is envisaged to contribute to an incremental volume change due to subsequent, sliding-induced rearrangement of grains and grain fragments. In general, time-dependent grain failure can be described either in a phenomenological way, using a static fatigue law for individual grains [e.g., Scholz, 1968] or based on fracture mechanics, by considering the growth criterion of the most fracture-prone crack in each grain [Brantut *et al.*, 2013].

In the latter case, it is implicit to the grain failure criterion that if all grains in the model pack were identical and contained identical surface flaws, simultaneous failure of all grains occurs at a fixed applied load [Brzesowsky *et al.*, 2011, 2014]. However, a more realistic representation is that grain failure is distributed through time, either due to the distributed nature of the flaw size at failure (denoted  $c_f$ ) or of the effective radius of curvature (denoted  $r_g$ ) at the grain-to-grain level, which affects the stress distribution within the aggregate (see Scholz [1968] and also Brzesowsky *et al.* [2011, 2014]). Similar to the time-independent model

previously presented by *Brzesowsky et al.* [2014], a time-dependent model for a population of grains would have to consider these two end-member cases: (i) spherical grains with constant radius of curvature plus a grain-to-grain distribution of  $c_f$  (assumed constant per grain) and (ii) nonspherical grains with constant  $c_f$ , plus a grain-to-grain distribution of effective radius of curvature  $r_g$ , representing contact asperity amplitude.

In order to avoid the uncertainty associated with the choice of a size distribution for initial flaw size and/or grain radius, we develop here a simplified analysis of a single crack growing from a stressed contact between two grains, which captures the essential features and trends of our data. Our analysis is based on the time-dependent deformation model presented by *Brzesowsky* [1995] (see chapter 5 therein). Let us consider an aggregate, consisting of brittle-elastic grains with grain size  $d$  ( $d = 2R$ , where  $R$  is the grain radius) and effective radius of curvature  $r_g$ , subjected to a remotely applied stress  $\sigma_a$ .

Within such an aggregate, Hertzian theory prescribes that the total normal load  $F$  exerted between two grains across a contact can be written as [*Huber, 1904*]

$$F = \frac{2\pi\sigma_0 a^2}{3} \quad (1)$$

where  $\sigma_0$  is the normal stress at the center of the contact. Alternatively,  $F$  can be expressed as  $\pi a^2 \sigma_n$  where  $\sigma_n$  is the mean normal contact stress. The radius of the contact disk between two grains  $a$  is described by the relation [*Johnson, 1987*]

$$a^3 = \frac{3Fr_g}{4E^*}, \quad (2)$$

where  $1/E^* = (1 - \nu_1^2)/E_1 + (1 - \nu_2^2)/E_2$  with  $\nu_i$  and  $E_i$  ( $i = 1, 2$ ) being the Poisson's ratio and the Young's moduli of the grains, respectively. When the grains that are in contact are of the same material, as in our case,  $E_1 = E_2$  and  $\nu_1 = \nu_2$ , so  $E^*$  reduces to  $E^* = E/[2(1 - \nu^2)]$ . In any ordered packing of grains with diameter  $d$ , the force balance condition prescribes the applied stress  $\sigma_a$  to be equal to

$$\sigma_a = \frac{\zeta \pi a^2 \sigma_n}{d^2} \quad (3)$$

where  $\zeta$  is a dimensionless, packing-dependent scaling factor that is equal to 1 for simple cubic packing, to  $2/\sqrt{3}$  for simple hexagonal packing, and to  $2/\sqrt{2}$  for face-centered cubic (FCC) packing. A simple hexagonal pack can be described in terms of a unit cell composed of two layers of vertically stacked spheres, with the spheres in each layer being located at the center and vertices of a hexagon. In an FCC pack, the constituent spheres are sited at the corners, and at the face centers, of a cubic unit cell with edge dimensions equal to  $\sqrt{2}d$ .

We assume that the grains contain preexisting surface flaws of initial dimension  $c_0$ . If  $c_0 \ll d$ , a flaw at the edge of the circular contact area can be considered as an edge crack subjected to the Hertzian maximum tensile radial stress [*Huber, 1904*]

$$\sigma_T = \frac{(1 - 2\nu)\sigma_0}{3}, \quad (4)$$

which implies that the crack tip stress is characterized by the mode I equivalent stress intensity factor

$$K_I = Y\sigma_T\sqrt{\pi c_0}, \quad (5)$$

where  $Y$  is a dimensionless factor equal to 1.12 for an edge crack [e.g., *Lawn, 1993*].

Making use of the relations for  $\sigma_0$  (equations (1) and (3)),  $a$  (equation (2)),  $\sigma_T$  (equation (4)), and  $K_I$  (equation (5)) given above, the mode I crack intensity factor at the crack tip, as a function of grain size and applied stress  $\sigma_a$ , is then given as

$$K_I = Y\sqrt{\pi c_0} \frac{1 - 2\nu}{2\pi\zeta^{1/3}} \left(\frac{4E^*}{3}\right)^{2/3} \left(\frac{d}{r_g}\right)^{2/3} \sigma_a^{1/3}. \quad (6)$$

In a time-independent framework, the propagation of the initial edge crack would be possible only when the Griffith equilibrium is reached, i.e., when  $K_I$  reaches the fracture toughness  $K_{Ic}$  of the material. However, at low homologous temperatures and in the presence of aqueous fluids, crack growth can occur in a subcritical manner at values of  $K_I$  substantially below the critical value  $K_{Ic}$  [e.g., *Lawn, 1993*].

Numerous rate descriptions have been formulated to describe subcritical crack growth, expressing crack growth velocity  $v_c$  as a function of  $K_I$  in the form of either empirical power laws [Atkinson, 1984; Atkinson and Meredith, 1987; Charles, 1958] or exponential laws derived from reaction rate theory [Bernabe and Brace, 1990; Chuang and Fuller, 1992; Cook, 1989; Darot and Gueguen, 1986; Wan et al., 1990]. Since the dependency of  $v_c$  on  $K_I$  is generally strong, typical laboratory crack growth experiments cannot distinguish between exponential and power laws, as they both fit the data equally well. For simplicity, we have chosen to use a general power law, of the form

$$v_c \propto K_I^n \quad (7)$$

where  $n$  is the so-called stress corrosion or subcritical crack growth index, which has been determined experimentally for quartz by Atkinson [1979] and Atkinson and Meredith [1981]. Experiments have shown that under dry conditions (air)  $n$  is approximately 40 and decreases significantly with increasing humidity to a value of  $\sim 12$  under fluid-saturated conditions (distilled water) [Atkinson, 1979; Atkinson and Meredith, 1981].

Grain failure is considered to contribute to an incremental volume change of the aggregate. The lifetime of a grain is approximately equal to the time required by a subcritical crack to reach a critical size, above which its growth becomes dynamic. Hence, in an aggregate composed of uniformly sized grains, the rate at which grains fail should be proportional to the average crack growth rate. Therefore, volumetric strain rate is thus directly proportional to crack growth rate, i.e.,  $\dot{\epsilon} \propto v_c$ . By combining equations (6) and (7) and accounting for the proportionality between volumetric strain and crack growth rate, we obtain

$$\dot{\epsilon} \propto C_0^{n/2} \sigma_a^{n/3} \left( \frac{d}{r_g} \right)^{2n/3} \quad (8)$$

If the grains are not perfectly spherical (case ii), the effective radius of curvature  $r_g$  is not directly proportional to the diameter  $d$  of the grain. Overall, equation (8) shows that any grain size sensitivity within our model arises from the nonsphericity of the grains, i.e., the presence of grain contact asperities.

Previous experiments performed on single sand grains, using the same sand as in the present study, have shown that  $r_g \propto d^{0.5-0.7}$  [Brzesowsky et al., 2011]. Furthermore, the present experimental data on dry quartz aggregates showed that  $\dot{\epsilon} \propto \sigma_a^{21} d^{4-8}$ , while under wet conditions  $\dot{\epsilon} \propto \sigma_a^{12-17} d^{6-11}$  (cf. section 3). Compared to the stress dependency expressed in equation (8) ( $n/3$ ), our observations would suggest a stress corrosion index  $n$  of approximately 60 under dry conditions and  $\sim 40$  under water wet conditions. These values are of the same order of magnitude and show the same trend as the measured values of  $n$  in crack growth tests [Atkinson, 1979, 1982; Atkinson and Meredith, 1981]. Using the values for the stress dependency, as determined in our experiments, i.e.,  $n=60$  for the dry case and  $n=40$  for the wet case, and accounting for  $r_g \propto d^{0.5-0.7}$ , we calculate that the grain size exponent should be of the order of 12–20 and 8–13 for the dry and wet cases, respectively. These values are of the correct order of magnitude, despite overestimating the grain size dependency for the dry case by a factor of about 2.

Overall, agreement between the simple model and our experimental observations is within a factor 2 for the stress and grain size exponents and reproduces the trends between dry and wet data. The discrepancies in the precise values for the exponents can arise from several reasons. First, it should be noted that the experimental determination of stress and grain size exponents is subject to significant imprecision, and the same can be said about the determination of stress corrosion indices during subcritical crack growth tests. Second, and most importantly, our expression for  $K_I$ , and hence for the crack growth rate, is valid only for cracks much smaller than the grain size (so that they can be approximated as edge cracks subjected to uniform tension). This assumption no longer holds as the cracks grow and their length become comparable to the grain size. In that sense, our estimate of crack growth rate, and inherently volumetric strain rate, corresponds to the early stages of crack growth within the grains. A complete calculation of  $K_I$  for larger crack sizes should include the determination of crack path and the effects of the stress on other contacts; such refinements are beyond the scope of our study.

## 8. Conclusions

Uniaxial compaction creep experiments performed on sands at room temperature, applied stresses in the range 14.5 to 30.0 MPa and under dry and wet conditions, for periods up to 24 days, have shown that time-dependent deformation behavior was dominated by subcritical transgranular cracking leading to grain failure, accompanied presumably by intergranular sliding rearrangements. The time-dependent grain

crushing process is clearly promoted by a chemically active pore fluid, by a higher pore fluid salinity, by a higher applied stress ( $\sigma_a$ ), and by a larger grain size ( $d$ ). In terms of a crude empirical power law formulation, the sensitivity of the compaction rate ( $\dot{\epsilon}$ ) of the sands to  $\sigma_a$  and  $d$  can be expressed as  $\dot{\epsilon} \propto \sigma_a^i d^j$  where  $i \approx 21$  and  $j \approx 6$  under dry conditions and  $i \approx 15$  and  $j \approx 9$  under wet conditions. The time-dependent cracking mechanism, in the presence of aqueous solutions, is inferred to be crack growth by stress corrosion probably involving cone crack growth under the action of Hertzian contact stresses until a critical crack size is reached. Acoustic emission (AE) events monitored during creep of the sands exhibited a near-linear relation between cumulative AE event counts and strain, suggesting a direct relation between progressive grain failure and strain. Moreover, the number of AE events counted per unit strain was found to be proportional to  $\sigma_a$  and  $1/d$ . This behavior has been explained in terms of a simple model in which whole grain failure events contribute to a strain increment proportional to  $d^3$  the number of AE events per failed grain is a direct function of  $\sigma_a$  and crack surface area scales with  $d^2$ . In addition, we compared our experimental results to a simple model based on Hertzian theory and linear elastic fracture mechanics. Agreement between the stress and grain size dependencies of creep as seen in our experiments and as predicted by the model is within a factor of 2.

### Notation

$a$	radius of contact circle between two grains.
$c_0$	initial flaw dimension.
$d$	mean grain size.
$E^*$	effective Young's modulus; $\frac{1}{E^*} = \frac{(1-\nu_1^2)}{E_1} + \frac{(1-\nu_2^2)}{E_2}$ .
$e_v$	volumetric strain.
$F$	total normal load transmitted between two grains.
$K_I$	stress intensity factor.
$K_{Ic}$	critical equivalent stress intensity factor.
$L_0$	initial sample length.
$\Delta L$	incremental change in sample length.
$n$	stress corrosion or subcritical crack growth index.
$R$	radius of the grains.
$r_g$	effective radius of curvature of a grain contact asperity.
$V_0$	initial solid volume.
$\Delta V$	incremental change in solid volume.
$v_c$	crack growth velocity.
$Y$	dimensionless factor, $Y \approx 1.12$ for a single-ended edge crack.

### Greek Symbols

$\alpha$	linear scaling factor.
$\dot{\epsilon}$	volumetric strain rate.
$\zeta$	linear scaling factor.
$\nu$	Poisson's ratio.
$\sigma_0$	normal stress at the center of the contact area.
$\sigma_a$	applied stress.
$\sigma_n$	normal contact stress.
$\sigma_T$	maximum tensile stress at the edge of the Hertzian contact.
$\phi_i$	initial porosity.

### Acknowledgments

R.H.B. was funded by a research grant from Royal Dutch Shell Exploration and Production, Rijswijk, Netherlands. We thank the Associate Editor and reviewer Antonino Cilona for constructive comments on our initial manuscript. Upon request to the corresponding author, the data used to support this article can be made available.

### References

- Anderson, O. L., and P. C. Grew (1977), Stress corrosion theory of crack propagation with applications to geophysics, *Rev. Geophys. Space Phys.*, *15*(1), 77–104.
- Atkinson, B. K. (1979), A fracture mechanics study of subcritical tensile cracking of quartz in wet environments, *Pure Appl. Geophys.*, *117*, 1011–1024.
- Atkinson, B. K. (1982), Subcritical crack propagation in rocks: Theory, experimental results and application, *J. Struct. Geol.*, *4*(4), 41–56.
- Atkinson, B. K. (1984), Subcritical crack growth in geological materials, *J. Geophys. Res.*, *89*(B6), 4077–4114, doi:10.1029/JB089iB06p04077.

- Atkinson, B. K., and P. G. Meredith (1981), Stress corrosion cracking of quartz: A note on the influence of chemical environment, *Tectonophysics*, *77*, T1–T11.
- Atkinson, B. K., and P. G. Meredith (1987), The theory of subcritical crack growth with applications to minerals and rocks, in *Fracture Mechanics of Rock*, edited by B. K. Atkinson, pp. 111–166, Academic Press, London, U. K.
- Bauer, S. J., and B. Johnson (1979), Effects of slow uniform heating on the physical properties of Westerly and Charcoal granites, paper presented at Proc. 20th US Symp. Rock Mech., Austin, Tex.
- Bernabe, Y., and W. F. Brace (1990), Deformation and fracture of Berea sandstone, in *The Brittle-Ductile Transition in Rocks*, edited by A. G. Duba et al., pp. 91–102, AGU, Washington, D. C.
- Brantut, N., P. Baud, M. J. Heap, and P. G. Meredith (2012), Micromechanics of brittle creep in rocks, *J. Geophys. Res.*, *117*, B08412, doi:10.1029/2012JB009299.
- Brantut, N., M. J. Heap, P. G. Meredith, and P. Baud (2013), Time-dependent cracking and brittle creep in crustal rocks: A review, *J. Struct. Geol.*, *52*, 17–43.
- Brzesowsky, R. H. (1995), Micromechanics of sand grain failure and sand compaction, PhD thesis, 180 pp., Utrecht Univ., Utrecht, Netherlands.
- Brzesowsky, R. H., C. J. Spiers, C. J. Peach, and S. J. T. Hangx (2011), Failure behavior of single sand grains: Theory versus experiment, *J. Geophys. Res.*, *116*, B06205, doi:10.1029/2010JB008120.
- Brzesowsky, R. H., C. J. Spiers, C. J. Peach, and S. J. T. Hangx (2014), Time-independent compaction behavior of quartz sands, *J. Geophys. Res. Solid Earth*, *119*, 936–956, doi:10.1002/2013JB010444.
- Charles, R. J. (1958), Static fatigue of glass. I, *J. Appl. Phys.*, *29*(11), 1549–1553.
- Chester, J. S., S. C. Lenz, F. M. Chester, and R. A. Lang (2004), Mechanisms of compaction of quartz sand at diagenetic conditions, *Earth Planet. Sci. Lett.*, *220*, 435–451.
- Chuang, T.-J., and E. R. Fuller (1992), Extended Charles-Hillig theory for stress corrosion cracking of glass, *J. Am. Ceram. Soc.*, *75*(3), 540–545.
- Chuhan, F. A., A. Kjeldstad, K. Bjørlykke, and K. Høeg (2002), Porosity loss in sand by grain crushing—Experimental evidence and relevance to reservoir quality, *Mar. Pet. Geol.*, *19*(1), 39–53.
- Chuhan, F. A., A. Kjeldstad, K. Bjørlykke, and K. Høeg (2003), Experimental compression of loose sands: Relevance to porosity reduction during burial in sedimentary basins, *Can. Geotech. J.*, *40*(5), 995–1011.
- Cook, R. F. (1989), Influence of crack velocity thresholds on stabilized nonequilibrium fracture, *J. Appl. Phys.*, *65*(5), 1902–1910.
- Costin, L. S. (1989), Time-dependent deformation and failure, in *Fracture Mechanics of Rock*, edited by B. K. Atkinson, pp. 167–215, Academic Press, London, U. K.
- Darot, M., and Y. Gueguen (1986), Slow crack growth in minerals and rocks: Theory and experiments, *Pure Appl. Geophys.*, *124*(4–5), 677–692.
- de Boer, R. B. (1977), Pressure solution: Theory and experiments, *Tectonophysics*, *39*(1–3), 287–301, doi:10.1016/0040-1951(77)90101-9.
- De Waal, J. A. (1986), *On the Rate Type Compaction Behavior of Sandstone Reservoir Rock*, 164 pp., Technische Hogeschool Delft, Delft, Netherlands.
- Donaldson, E. C., G. V. Chilingarian, and H. H. Rieke (1995), Stresses in sediments, in *Subsidence Due To Fluid Withdrawal*, edited by G. V. Chilingarian, E. C. Donaldson, and T. F. Yen, pp. 165–192, Elsevier Science, Amsterdam, Netherlands.
- Doornhof, D., T. G. Kristiansen, N. B. Nagel, P. D. Patillo, and C. Sayers (2006), Compaction and subsidence, *Oilfield Review*, *Autumn*, *18*(3), 50–68.
- Dove, P. M. (1994), The dissolution of quartz in sodium chloride solutions at 25° to 300°C, *Am. J. Sci.*, *294*, 665–712.
- Dove, P. M. (1995), Geochemical controls on the kinetics of quartz fracture at subcritical tensile stresses, *J. Geophys. Res.*, *100*(B11), 22,349–22,359, doi:10.1029/95JB02155.
- Dove, P. M., and S. F. Elston (1992), Dissolution kinetics of quartz in sodium chloride solutions: Analysis of existing data and a rate model for 25°C, *Geochim. Cosmochim. Acta*, *56*, 4147–4156.
- Dunning, J., B. Douglas, M. Miller, and S. McDonald (1994), The role of the chemical environment in frictional deformation: Stress corrosion cracking and comminution, *Pure Appl. Geophys.*, *143*, 151–178.
- Elias, B. P., and A. Hajash (1992), Changes in quartz solubility and porosity due to effective stress: An experimental investigation of pressure solution, *Geology*, *20*(5), 451–454.
- Fisk, G. A., and T. A. Michalske (1985), Laser-based and thermal studies of stress corrosion in vitreous silica, *J. Appl. Chem.*, *58*(7), 2736–2741.
- Gratz, A. J., and P. Bird (1993a), Quartz dissolution: Negative crystal experiments and a rate law, *Geochim. Cosmochim. Acta*, *57*(5), 965–976.
- Gratz, A. J., and P. Bird (1993b), Quartz dissolution: Theory of rough and smooth surfaces, *Geochim. Cosmochim. Acta*, *57*(5), 977–989.
- Hangx, S. J. T., C. J. Spiers, and C. J. Peach (2010), Creep of simulated reservoir sands and coupled chemical-mechanical effects of CO<sub>2</sub> injection, *J. Geophys. Res.*, *115*, B09205, doi:10.1029/2009JB006939.
- Heap, M. J., P. Baud, P. G. Meredith, A. F. Bell, and I. G. Main (2009), Time-dependent brittle creep in Darley Dale sandstone, *J. Geophys. Res.*, *114*, B07203, doi:10.1029/2008JB006212.
- Hettema, M., E. Papamichos, and P. M. T. M. Schutjens (2002), Subsidence delay: Field observations and analysis, *Oil Gas Sci. Technol.*, *57*(5), 443–458.
- Hicks, B. D. (1989), *Dissolution of Experimentally Compacted Quartz Sand*, Univ. of Missouri-Columbia, Columbia, Mo.
- Hiemstra, T., and W. H. van Riemsdijk (1990), Multiple activated complex dissolution of metal (hydr)oxides: A thermodynamic approach applied to quartz, *J. Colloid Interface Sci.*, *136*(1), 132–150.
- Huber, M. T. (1904), Zur Theorie der Berührung fester elastischer Körper, *Ann. Phys.*, *319*(6), 153–163.
- Johnson, K. L. (1987), *Contact Mechanics*, Cambridge Univ. Press, Cambridge, U. K.
- Karig, D. E., and G. Hou (1992), High-stress consolidation experiments and their geologic implications, *J. Geophys. Res.*, *97*(B1), 289–300, doi:10.1029/91JB02247.
- Karner, S. L., J. S. Chester, F. M. Chester, A. K. Kronenberg, and A. Hajash Jr. (2005), Laboratory deformation of granular quartz sand: Implications for the burial of clastic rocks, *AAPG Bull.*, *89*(5), 603–625, doi:10.1306/12200404010.
- Lambe, T. W., and R. V. Whitman (1979), *Soil Mechanics, SI Version*, Wiley, New York.
- Lawn, B. R. (1993), *Fracture of Solids*, 2nd ed., Cambridge Univ. Press, Cambridge, U. K.
- Liu, Z., L. R. Myer, and N. G. W. Cook (1993), Micromechanics of granular materials—Numerical simulation of the effects of heterogeneities, *Int. J. Rock Mech. Min. Sci. Geomech. Abstr.*, *30*(7), 1281–1284.
- Lysak, M. V. (1994), Acoustic emission during jumps in subcritical growth of cracks in three-dimensional bodies, *Eng. Fract. Mech.*, *47*(6), 873–879.
- Main, I., and P. G. Meredith (1991), Stress corrosion constitutive laws as a possible mechanism of intermediate-term and short-term seismic quiescence, *Geophys. J. Int.*, *107*, 363–372.
- Michalske, T. A., and B. C. Bunker (1987), Steric effects in stress corrosion fracture of glass, *J. Am. Chem. Soc.*, *70*(10), 780–784.
- Michalske, T. A., and S. W. Freiman (1982), A molecular interpretation of stress corrosion in silica, *Nature*, *295*(5849), 511–512.
- Morey, G. W., R. O. Fournier, and J. J. Rowe (1962), The solubility of quartz in water in the temperature interval from 25° to 300° C, *Geochim. Cosmochim. Acta*, *26*(10), 1029–1043.

- Renard, F., A. Park, P. Ortoleva, and J.-P. Gratier (1999), An integrated model for transitional pressure solution in sandstones, *Tectonophysics*, 312, 97–115.
- Rimstidt, J. D., and H. L. Barnes (1980), The kinetics of silica-water reactions, *Geochim. Cosmochim. Acta*, 44(11), 1683–1699.
- Robie, R. A., B. S. Hemingway, and J. R. Fisher (1978), Thermodynamic properties of minerals and related substances at 298.15 K and 1 bar ( $10^5$  Pa) pressure and at higher temperatures, *U.S. Geol. Surv. Bull.*, 1452.
- Scholz, C. H. (1968), Mechanism of creep in brittle rock, *J. Geophys. Res.*, 73(10), 3295–3302, doi:10.1029/JB073i010p03295.
- Schutjens, P. M. T. M. (1991a), Experimental compaction of quartz sand at low effective stress and temperature conditions, *J. Geol. Soc.*, 148(3), 527–539, doi:10.1144/gsjgs.148.3.0527.
- Schutjens, P. M. T. M. (1991b), Intergranular pressure solution in halite aggregates and quartz sands: An experimental investigation, PhD thesis, 233 pp., Utrecht Univ., Utrecht, Netherlands.
- Schutjens, P. M. T. M., H. de Ruig, and J. G. van Munster (1994), Compressibility measurement and acoustic characterisation of quartz-rich consolidated reservoir rock (Brent Field, North Sea), in *Eurock '94—Rock Mechanics In Petroleum Engineering*, Proceedings of the SPE/ISRM International Conference, edited, pp. 557–571, A.A. Balkema, Rotterdam, Delft, Netherlands.
- Schutjens, P. M. T. M., T. W. Fens, and R. M. M. Smits (1995), Experimental observations of the uniaxial compaction of quartz-rich reservoir rock at stresses up to 80 MPa, paper presented at 5th International Symposium on Land Subsidence, IAHS Press, Institute of Hydrology, The Hague, Netherlands, 16–20 Oct.
- Sone, H., and M. D. Zoback (2010), Strength, creep and frictional properties of gas shale reservoir rocks, paper presented at 44th U.S. Rock Mechanics Symposium and 5th U.S.-Canada Rock Mechanics Symposium, edited, Am. Rock Mech. Assoc., Salt Lake City, Utah.
- Walther, J. V., and H. C. Helgeson (1977), Calculation of the thermodynamic properties of aqueous silica and the solubility of quartz and its polymorphs at high pressures and temperatures, *Am. J. Sci.*, 277(10), 1315–1351.
- Wan, K.-T., S. Lthabai, and B. R. Lawn (1990), Crack velocity functions and thresholds in brittle solids, *J. Eur. Ceram. Soc.*, 6(4), 259–268.
- Wiederhorn, S. M., and L. H. Bolz (1970), Stress corrosion and static fatigue of glass, *J. Am. Ceram. Soc.*, 53(10), 543–548.
- Xiao, Y., and A. C. Lasaga (1994), Ab initio mechanical studies of the kinetics and mechanisms of silicate dissolution:  $H^+$  ( $H_3O^+$ ) catalysis, *Geochim. Cosmochim. Acta*, 58(24), 5379–5400.
- Zhang, J., T.-F. Wong, and D. M. Davis (1990a), Micromechanics of pressure-induced grain crushing in porous rocks, *J. Geophys. Res.*, 95(B1), 341–352, doi:10.1029/JB095iB01p00341.
- Zhang, J., T.-F. Wong, T. Yanagidani, and D. M. Davis (1990b), Pressure-induced microcracking and grain crushing in Berea and Boise sandstones: Acoustic emission and quantitative microscopy measurements, *Mech. Mater.*, 9(1), 1–15.